



Tracing the Ionization Structure of the Shocked Filaments of NGC 6240

Anne M. Medling^{1,2,3,4,21}, Lisa J. Kewley^{2,4}, Daniela Calzetti⁵, George C. Privon^{6,7}, Kirsten Larson^{3,8}, Jeffrey A. Rich⁹, Lee Armus¹⁰, Mark G. Allen¹¹, Geoffrey V. Bicknell², Tanio Díaz-Santos^{12,13}, Timothy M. Heckman¹⁴, Claus Leitherer¹⁵, Claire E. Max¹⁶, David S. N. Rupke¹⁷, Ezequiel Treister¹⁸, Hugo Messias¹⁹, and Alexander Y. Wagner²⁰

¹ Ritter Astrophysical Research Center, University of Toledo, Toledo, OH 43606, USA; anne.medling@utoledo.edu

² Research School of Astronomy & Astrophysics, Mount Stromlo Observatory, Australia National University, Cotter Road, Weston, ACT 2611, Australia

³ Cahill Center for Astronomy & Astrophysics, California Institute of Technology, 1200 E. California Blvd., Pasadena, CA 91125, USA

⁴ ARC Centre of Excellence for All Sky Astrophysics in 3 Dimensions (ASTRO 3D), Australia

⁵ Department of Astronomy, University of Massachusetts, Amherst, Amherst, MA 01003, USA

⁶ National Radio Astronomy Observatory, 520 Edgemont Rd, Charlottesville, VA 22903, USA

⁷ Department of Astronomy, University of Florida, 211 Bryant Space Sciences Center, Gainesville, FL 32611, USA

⁸ AURA for the European Space Agency (ESA), Space Telescope Science Institute, 3700 San Martin Drive, Baltimore, MD 21218, USA

⁹ The Observatories of the Carnegie Institution for Science, 813 Santa Barbara St., Pasadena, CA 91101, USA

¹⁰ Infrared Processing and Analysis Center, California Institute of Technology, Pasadena, CA 91125, USA

¹¹ Université de Strasbourg, CNRS, Observatoire astronomique de Strasbourg, UMR 7550, F-67000 Strasbourg, France

¹² Institute of Astrophysics, Foundation for Research and Technology - Hellas (FORTH), Heraklion, GR-70013, Greece

¹³ Núcleo de Astronomía de la Facultad de Ingeniería y Ciencias, Universidad Diego Portales, Av. Ejército Libertador 441, Santiago, Chile

¹⁴ Department of Physics & Astronomy, Johns Hopkins University, Baltimore, MD 21218, USA

¹⁵ Space Telescope Science Institute, 3700 San Martin Dr, Baltimore, MD 21218, USA

¹⁶ Department of Astronomy & Astrophysics, University of California, Santa Cruz, CA 95064, USA

¹⁷ Department of Physics, Rhodes College, Memphis, TN 38112, USA

¹⁸ Instituto de Astrofísica, Facultad de Física, Pontificia Universidad Católica de Chile, Casilla 306, Santiago 22, Chile

¹⁹ Joint ALMA Observatory and European Southern Observatory, Alonso de Córdova 3107, Casilla 19001, Vitacura, Santiago, Chile

²⁰ Center for Computational Sciences, University of Tsukuba, 1-1-1 Tennodai, Tsukuba, Ibaraki 305-8577, Japan

Received 2019 July 9; revised 2021 September 22; accepted 2021 October 9; published 2021 December 20

Abstract

We study the ionization and excitation structure of the interstellar medium in the late-stage gas-rich galaxy merger NGC 6240 using a suite of emission-line maps at ~ 25 pc resolution from the Hubble Space Telescope, Keck/NIRC2 with Adaptive Optics, and the Atacama Large Millimeter/submillimeter Array (ALMA). NGC 6240 hosts a superwind driven by intense star formation and/or one or both of two active nuclei; the outflows produce bubbles and filaments seen in shock tracers from warm molecular gas (H_2 2.12 μm) to optical ionized gas ([O III], [N II], [S II], and [O I]) and hot plasma (Fe XXV). In the most distinct bubble, we see a clear shock front traced by high [O III]/H β and [O III]/[O I]. Cool molecular gas (CO(2–1)) is only present near the base of the bubble, toward the nuclei launching the outflow. We interpret the lack of molecular gas outside the bubble to mean that the shock front is not responsible for dissociating molecular gas, and conclude that the molecular clouds are partly shielded and either entrained briefly in the outflow, or left undisturbed while the hot wind flows around them. Elsewhere in the galaxy, shock-excited H_2 extends at least ~ 4 kpc from the nuclei, tracing molecular gas even warmer than that between the nuclei, where the two galaxies' interstellar media are colliding. A ridgeline of high [O III]/H β emission along the eastern arm aligns with the southern nucleus' stellar disk minor axis; optical integral field spectroscopy from WiFeS suggests this highly ionized gas is centered at systemic velocity and likely photoionized by direct line of sight to the southern active galactic nucleus.

Unified Astronomy Thesaurus concepts: Galactic winds (572); Luminous infrared galaxies (946); Galaxy mergers (608); Shocks (2086); Superbubbles (1656)

1. Introduction

Local ultra- and luminous infrared galaxies (U/LIRGs, with $\log(L_{\text{IR}}/L_{\odot}) \geq 12$ and 11, respectively) provide a useful probe of the energetic processes that shaped galaxies over cosmic time. The high infrared luminosities of U/LIRGs are produced by dust heated by a combination of star formation and active galactic nucleus (AGN) activity (e.g., Sanders & Mirabel 1996). In the local universe, these extreme infrared luminosities occur

most commonly in gas-rich major mergers (Veilleux et al. 2002), although mergers may not be required to trigger the same high star formation rates (SFRs) and AGN luminosities at $z \sim 2$ (Kartaltepe et al. 2010, 2012). To understand the evolutionary processes of galaxies at cosmic noon ($z \sim 1$ –3, when star formation and AGN energy densities peaked; Madau et al. 1998; Aird et al. 2010), it is beneficial to study the detailed energetics of local galaxies with similar SFRs and AGN luminosities: U/LIRGs.

Emission-line fluxes and ratios are powerful probes of the physical processes present in a galaxy. Ratios of the optical emission lines [O III]/H β , [N II]/H α , [S II]/H α , and [O I]/H α can be used to distinguish between possible ionization mechanisms of gas using the BPT/VO87 line diagnostic diagrams (Baldwin et al. 1981; Veilleux & Osterbrock 1987).

²¹ Hubble Fellow.

Original content from this work may be used under the terms of the Creative Commons Attribution 4.0 licence. Any further distribution of this work must maintain attribution to the author(s) and the title of the work, journal citation and DOI.

Although these diagnostic diagrams were originally used to differentiate between gas photoionized by H II regions and by AGN, recent models of fast (200–1000 km s⁻¹; Allen et al. 2008) and slow (100–200 km s⁻¹; Rich et al. 2010, 2011) shocks have shown that the ionization mechanisms of galaxies are more complex. For example, a galaxy containing star formation or AGN activity driving a wind may contain collisionally ionized shocked gas, increasing its line ratios into the AGN or LINER regions of diagnostic diagrams even if the photoionized gas shows lower line ratios. For this reason, enhanced line ratios tracing shocks are now commonly associated with galactic winds (e.g., Ho et al. 2014). Near-infrared emission lines such as [Fe II] and the rovibrational H₂ transitions around 2.2 μm are also excited by outflows (van der Werf et al. 1993; Veilleux et al. 2009; Hill & Zakamska 2014). The interstellar media of galaxies must be clumpy and multiphase for a single wind to shock both molecular and ionized gas, because the shock velocities seen in ionized gas are fast enough to dissociate H₂ (>25 km s⁻¹; Hollenbach & McKee 1980). Investigating shocks with multiple tracers is, therefore, required to fully understand the energy budget associated with galactic feedback.

NGC 6240 ($16^{\text{h}}52^{\text{m}}58\overset{\text{s}}{.}9 +02^{\text{d}}24^{\text{m}}03\overset{\text{s}}{.}$, $z = 0.0243$, $\log(L_{\text{IR}}/L_{\odot}) = 11.93$; Kim et al. 2013) is a particularly complex case study of shocks and shock drivers. It hosts two X-ray confirmed AGN separated by 735 pc (1''.5) (Komossa et al. 2003; Max et al. 2007), is forming stars at up to $140 M_{\odot} \text{ yr}^{-1}$ (Heckman et al. 1990), and is driving a superwind seen in radio (Baan et al. 2007), far-infrared (Veilleux et al. 2013), near-infrared (van der Werf et al. 1993; Max et al. 2005), optical (Heckman et al. 1990; Veilleux et al. 2003), and X-ray (Nardini et al. 2013; Wang et al. 2014) observations. Although NGC 6240's two nuclei both host AGN, the nuclei may be too weak or buried to dominate the ionization of the interstellar medium (ISM); star formation accounts for 76%–80% of the infrared luminosity (Armus et al. 2006). Star formation appears to be driving the outflow, which originates in the southern nucleus (Baan et al. 2007) and produces shock velocities up to the 2200 km s⁻¹ required to emit the diffuse hard X-ray photons (Wang et al. 2014). Roughly $3 \times 10^9 M_{\odot}$ of molecular gas is present in a tidal bridge between the two nuclei (Tacconi et al. 1999; Engel et al. 2010). The majority of molecular line emission is seen in this region and likely comes from C-shocks with $v_{\text{shock}} = 20\text{--}40 \text{ km s}^{-1}$ produced by the collision of the interstellar media of the two galaxy nuclei (van der Werf et al. 1993). Shocked molecular gas is also present in the superwind, demonstrated by the filaments of H₂ (Max et al. 2005) and CO emission (Feruglio et al. 2013a, 2013b) tracing the ionized gas emission features. Feruglio et al. (2013a) estimates that $100\text{--}500 M_{\odot} \text{ yr}^{-1}$ of molecular gas is expelled by this outflow.

In this paper, we present high spatial resolution ($\sim 50 \text{ mas} = 24.5 \text{ pc}$) maps of the inner few kiloparsecs of NGC 6240 highlighting key optical, near-infrared, and submillimeter emission lines, from narrowband imaging and 3D spectroscopy. This unique combined data set offers the most comprehensive view to date of the structure of the ISM in a galaxy hosting AGN, star formation, outflows, and shocks. In Section 2, we describe our data and data processing techniques. We compare the fluxes and morphologies of emission lines in Section 3 and discuss their physical implications in Sections 4–6. In Section 7, we summarize our conclusions. Throughout the paper we adopt $H_0 = 70 \text{ km s}^{-1} \text{ Mpc}^{-1}$,

Table 1
Narrowband Imaging Emission-line Content

Filter	Exp. Time (s)	Spectral Range (nm)	Included Strong Emission Lines
HST WFC3	Proposal ID: 12552		
F467M	1540	458.25–478.35	...
FQ492N	5490 ^a	487.6–499.9	H β
FQ508N	5490 ^a	502.55–515.65	[O III]
F621M	310	591.45–652.35	[O I]
F645N	2358	641.2–649.6	[O I]
F673N	390	670.7–682.5	H α , [N II]
F680N	1050	669.19–706.25	H α , [N II], [S II]
	Proposal ID: 13690		
F130N	5383	1292.8–1308.4	...
F132N	5383	1310.75–1326.85	Pa β
HST ACS	Proposal ID: 10592		
F814W	720	773.1–838.3	...
Keck/NIRC2			
Br γ	1200	2152.3–2184.9	H ₂
H ₂ ^b	1200	2111.2–2145.2	...

Notes.

^a Two additional frames totalling 2160 and 2090 s for each of FQ492N and FQ508N, respectively, exist but were excluded from the analysis due to excessive cosmic rays.

^b This filter was formerly incorrectly labeled “NB2108” in the vendor documentation.

$\Omega_m = 0.28$, and $\Omega_{\Lambda} = 0.72$ (Hinshaw et al. 2009). The physical scale is thus $490 \text{ pc arcsec}^{-1}$, calculated using Ned Wright’s Cosmology Calculator²² (Wright 2006).

2. Observations

2.1. Imaging

2.1.1. Hubble Space Telescope Imaging

We used a combination of narrow-, medium-, and broadband optical images from the Hubble Space Telescope’s Wide-Field Camera 3 (WFC3) and Advanced Camera for Surveys (ACS) to isolate key emission lines. Most optical images were observed in Cycle 19 (Proposal ID: 12552, PI: L. Kewley); the F814W image was observed in Cycle 14 (Proposal ID: 10592, PI: A. Evans); images in the 1–2 μm range were observed in Cycle 22 (Proposal ID: 13690, PI: T. Diaz-Santos). Details of these observations are listed in Table 1. The fully reduced and calibrated images from ACS and WFC3/UVIS were downloaded from the Barbara A. Mukulski Archive for Space Telescopes in 2019 January. The WFC3/IR images (F130N and F132N) were specifically regridded and processed as described in Larson et al. (2020) before our analysis.

2.1.2. Keck/NIRC2 Adaptive Optics Imaging

We also make use of Keck Adaptive Optics (AO) narrowband imaging with the NIRC2 camera (PI: K. Matthews) around 2.2 μm. These images were initially presented in Max et al. (2005). The Keck II AO system (Wizinowich et al. 2000; van Dam et al. 2004) used a natural guide star ($R = 11.9$, $B = 13.5$, and separation = 35''.8) and a deformable mirror to measure and correct for atmospheric

²² Available at <http://www.astro.ucla.edu/~wright/CosmoCalc.html>.

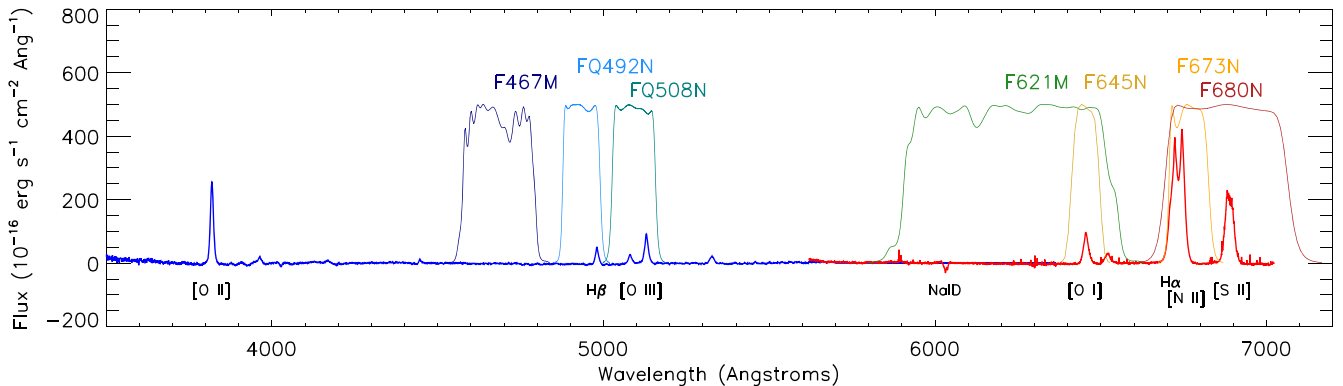


Figure 1. Representative optical spectrum of NGC 6240 integrated over our WiFeS field of view showing the blue (wavelength $< 5800 \text{ \AA}$) and red (wavelength $> 5700 \text{ \AA}$) arms, with total HST system throughput curves of relevant WFC3/UVIS filters overlaid.

turbulence and provide near diffraction-limited image resolution. Isolated star clusters in the image show a full width at half max of $0''.14$, an upper limit on our achieved spatial resolution. The imaging presented here uses the wide camera ($0''.04 \text{ pixel}^{-1}$), a good match to the ACS imaging plate scale ($0''.05 \text{ pixel}^{-1}$). No observations of photometric standards were taken with NIRCam during this run; to flux calibrate the data, we used archival NICMOS imaging of star clusters in the field similar narrowband filters.

2.1.3. Registering the Images

We registered all images to match the F621M filter coordinates using the IRAF routines geomap and geotran. We used the coordinates of isolated nonsaturated stars (typically 15–25 per filter) as inputs to the geomap routine; this number is sufficient to determine the translational shift, rotation, and distortion corrections for the WFC3 camera.

2.1.4. Line Maps

Careful continuum subtraction is critical to producing meaningful emission-line maps from narrowband imaging, particularly in a galaxy with high dust extinction like NGC 6240 (global $A_V \sim 15\text{--}20$ mag; Lutz et al. 2003). We counteract this by producing clean continuum maps in three bracketing wavelength bands; the final continuum subtraction for each filter is calculated by interpolating the continuum spectrum smoothly between continuum maps.

Figure 1 shows a representative optical spectrum of NGC 6240 from our WiFeS data (see Section 2.2.1) with the relevant throughput curves for each HST filter overlaid. The throughput curves are the most up-to-date version as of 2018 May 31.²³ The F467M filter is clean of strong emission lines; we use it as the blue continuum map. The F814W filter is broad (65.2 nm wide) and contains relatively few emission lines. We estimate the emission-line contamination of the F814W is $<1\%$, and use it as the reddest continuum map. We also use the combination of F621M and F645N images (which both contain only [O I]) to create an intermediate continuum map for better interpolation, with the following iterative procedure:

- With F621M and F645N images in $\text{erg s}^{-1} \text{cm}^{-2} \text{\AA}^{-1}$, the [O I] contribution to the medium-band filter is significantly lower. We use it to provide a first estimate of the

continuum and create an initial [O I] map.

$$\text{map}_{[\text{O I}],0} = \text{F645N} - \text{F621M}$$

- Because this [O I] map estimate is in $\text{erg s}^{-1} \text{cm}^{-2} \text{\AA}^{-1}$, we scale it by the ratio of bandwidths and subtract it from the medium-band filter to obtain a cleaned continuum map.

$$\text{map}_{\text{cont},1} = \text{F621M} - \text{map}_{[\text{O I}],0} \times \frac{\Delta\lambda_{\text{F645N}}}{\Delta\lambda_{\text{F621M}}}$$

- With this improved continuum estimate, we produce a cleaned [O I] map.

$$\text{map}_{[\text{O I}],1} = \text{F645N} - \text{map}_{\text{cont},1}$$

- We iterate again to confirm the [O I] map is stable:

$$\text{map}_{\text{cont},2} = \text{F621M} - \text{map}_{[\text{O I}],1} \times \frac{\Delta\lambda_{\text{F645N}}}{\Delta\lambda_{\text{F621M}}}$$

$$\text{map}_{[\text{O I}],2} = \text{F645N} - \text{map}_{\text{cont},2}$$

- The differences between the second and first iteration of $\text{map}_{[\text{O I}]}$ is approximately 5% of the image’s 1σ uncertainty level, which we find sufficient. Because $\text{map}_{[\text{O I}],2} \approx \text{map}_{[\text{O I}],1}$, we are confident in our continuum subtraction, and adopt $\text{map}_{\text{cont},2}$ as a clean continuum map at intermediate wavelengths. We multiply $\text{map}_{[\text{O I}],2}$ by the bandwidth of F645N to produce a final [O I] line map in units of $\text{erg s}^{-1} \text{cm}^{-2}$.

To produce the H β and [O III] line maps, we interpolate between the F467M clean continuum and the continuum from the cleaned F621M image to the appropriate wavelength. Our final line maps have this continuum subtracted, and are then multiplied by the relevant bandwidth in order to recover the units of $\text{erg s}^{-1} \text{cm}^{-2}$. A map of H α +[N II] is constructed in the same way, using a continuum interpolated between that of the F621M filter and the F814W filter. To produce the [S II] line map (which for this paper always refers to the sum of the fluxes of the [S II] $\lambda\lambda 6716, 6731$ doublet), we subtract off both the continuum and the H α +[N II] contribution from the F680N filter. Note that Balmer emission lines are, therefore, *not* corrected for stellar absorption. Based on the spectroscopy described in Section 2.2.1, we estimate the effect of stellar absorption at the $<15\%$ level in H β across most of the galaxy; in a few percent of spaxels, the Balmer absorption correction can be as high as 50% for H β . The deep stellar absorption, therefore, contributes to the low signal-to-noise ratio (S/N) seen in our H β map, particularly around the nuclei. Maps of H β

²³ Throughput curves were downloaded from http://www.stsci.edu/hst/wfc3/ins_performance/throughputs/Throughput_Tables.

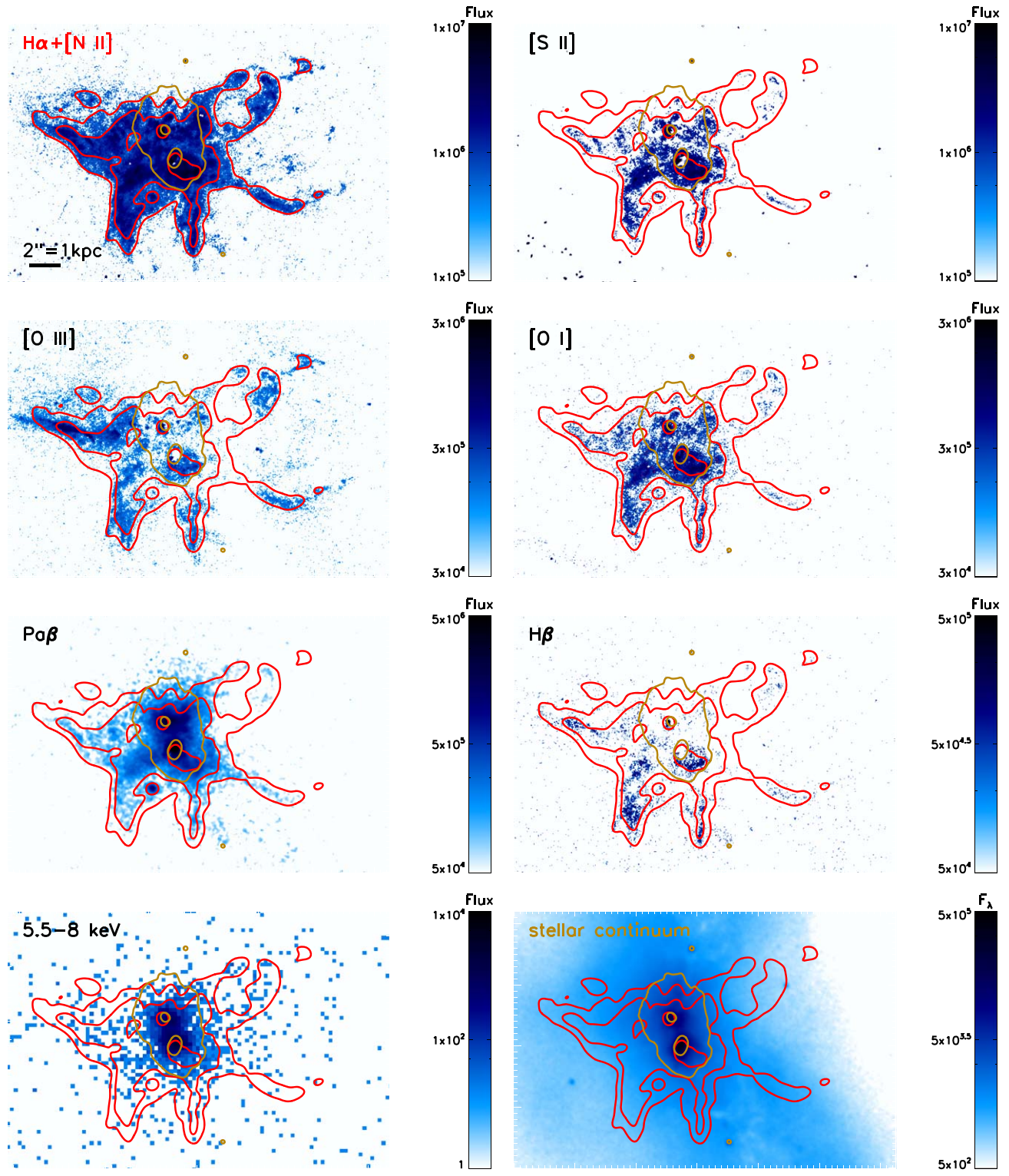
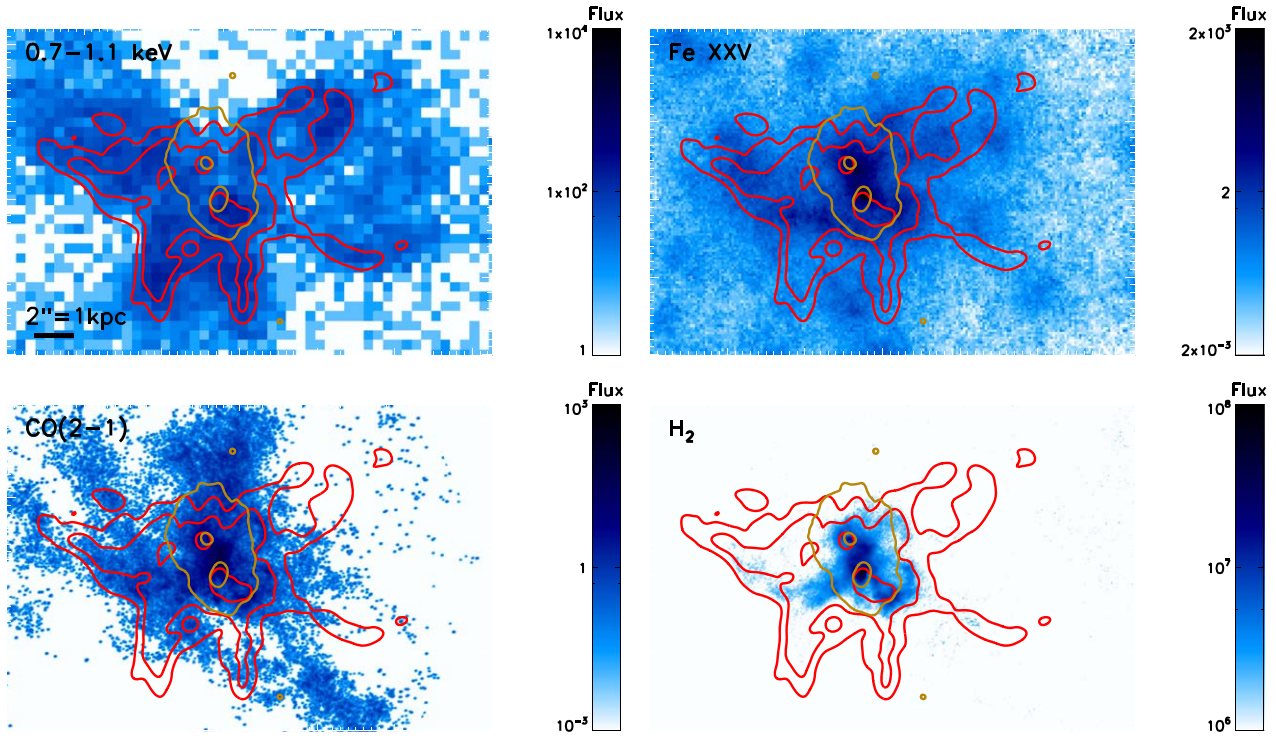


Figure 2. Maps of emission lines H α +[N II], [S II], [O III], [O I], Pa β , H β , H $_2$ 1–0 S(1), CO(2–1), Fe XXV, hard and soft X-rays, and the stellar continuum from the F130N WFC3 filter. Each panel is shown in log scale with limits chosen to emphasize structure, and has H α +[N II] contours (red) and stellar continuum contours (brown) overlaid for comparison. Optical/NIR line emission flux maps are shown in units of 10^{-20} erg s $^{-1}$ cm $^{-2}$ arcsec $^{-2}$, and the stellar continuum flux map is shown in units of 10^{-20} erg s $^{-1}$ cm $^{-2}$ Å $^{-1}$ arcsec $^{-2}$. The X-ray maps are shown in units of counts arcsec $^{-2}$, and the CO(2–1) map is shown in units of Jy beam $^{-1}$ km s $^{-1}$. The scale bar in the top left panel shows 2''.05, approximately one kiloparsec.

equivalent width (of the continuum and the overall data) from our integral field spectroscopy are shown in Appendix.

Both near-infrared line maps (Pa β and H $_2$) come from a matched pair of filters: one containing the line and one

containing the nearby continuum. As above, the line images have the continuum contribution removed and are then multiplied by the relevant bandwidth to present the line flux in units of erg s $^{-1}$ cm $^{-2}$. Maps and contours of stellar

**Figure 2.** (Continued.)

continuum in figures below use the F130N image, because the reddest line-free image is least affected by dust.

Due to the presence of noise in the images, we mask out flux that is below the 3σ level. The noise level of each line map is given as the standard deviation of pixel values in an off-galaxy region $4''$ by $4''$ in size, $30''$ from the nucleus at 100° east of north. Final line maps are shown in Figure 2 and discussed in the following sections.

2.2. Spatially Resolved Spectroscopy

We also incorporate optical integral field spectroscopy (IFS) of NGC 6240 into our analysis to estimate the [N II]/H α ratios and to provide kinematic interpretations in later sections, Band 6 interferometry from the Atacama Large Millimetre Array (ALMA) to map the CO(2–1) cold gas emission, and Chandra X-ray observations to trace hot gas.

2.2.1. Integral Field Spectroscopy from the Wide-field Spectrograph on the ANU 2.3 m Telescope

We use observations of NGC 6240 from WiFeS on the ANU 2.3 m Telescope at the Siding Spring Observatory, taken in 2014 July, with 10 minute frames taken at a ratio of approximately three target frames to one sky frame, totaling 120 minutes on source. WiFeS (Dopita et al. 2007, 2010) is a dual-arm image slicer that, in this mode, covers 3700–5700 Å at a spectral resolution of $R \sim 3000$ and 5700–7000 Å at $R \sim 7000$; WiFeS frames cover an area of $25'' \times 36''$, with $1''$ spatial sampling. During these observing runs, the seeing was approximately $1''.5$.

Our WiFeS data were reduced using the standard PyWiFeS pipeline v0.6.0 (Childress et al. 2014). The resulting blue and red data cubes were median-combined and then analyzed using

LZIFU (Ho et al. 2016), an IDL package that uses penalized pixel fitting (pPXF; Cappellari & Emsellem 2004) to fit the stellar continuum and then MPFIT (Markwardt 2009) to fit one, two, or three Gaussian components to each of 11 strong emission lines simultaneously. Across most of the field of view, the line profiles are extremely complex, and a standard f-test recommends using all three Gaussian components. Therefore, we estimate the [N II]/H α ratio in Section 3 using the sum of all three components for each line.

Select lines and line ratios are presented in the main body of the text where higher spatial resolution HST data are unavailable, but the entire set of emission-line maps is presented in the Appendix for completeness.

2.2.2. Band 6 Interferometry from ALMA

We present new long-baseline imaging of CO(2–1) from the Atacama Large Millimetre Array (ALMA). This Band 6 observation was taken as part of program 2015.1.00370.S (PI: Treister) in three blocks between 2015 November and 2016 May for an aggregate exposure time of approximately 4600 s and has a resolution of $0''.06 \times 0''.03$. To improve the coverage of larger-scale structure, the data from program 2015.1.00003.S (PI: Saito; Saito et al. 2018) were also included.

These data provide the highest resolution view of the cold molecular gas to date, which we contrast with other phases of the ISM at similar spatial resolutions in this paper. A complete analysis of the CO(2–1) and Band 6 continuum data set is presented in Treister et al. (2020).

2.2.3. Chandra X-Ray Observatory Data

We make use of deep X-ray observations from the Chandra X-ray Observatory, originally published in Nardini et al. (2013)

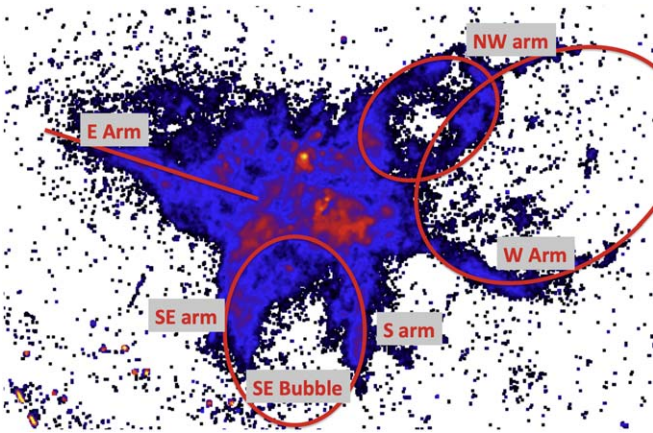


Figure 3. Map of $\text{H}\alpha + [\text{N II}]$ from Figure 2 with schematic identification of the filamentary and bubble features referred to throughout this work.

and Wang et al. (2014) and graciously provided by those authors in their processed forms. The observations are comprised of ~ 150 ks of integration using the Chandra Advanced CCD Imaging Spectrometer (ACIS; Garmire et al. 2003). Here we present the hard X-ray continuum (5.5–8 keV) and Fe XXV emission-line maps from Wang et al. (2014) and the soft X-ray continuum (0.7–1.1 keV) map from Nardini et al. (2013). All three are tracers of hot gas likely associated with winds.

3. Results: Emission Lines and Ratios

3.1. Emission-line Structure

In Figure 2, we present flux maps of the key emission lines $\text{H}\alpha + [\text{N II}]$, $[\text{S II}]$, $[\text{O III}]$, $[\text{O I}]$, $\text{Pa}\beta$, $\text{H}\beta$, the near-infrared stellar continuum from HST, the hard and soft X-ray continuum and the Fe XXV line from Chandra, the warm H_2 emission from Keck, and the CO(2–1) emission from ALMA. All emission lines presented in Figure 2 show a filamentary and/or bubble structure associated with the superwinds and merger disruptions known to be present in NGC 6240. The $\text{H}\alpha + [\text{N II}]$ emission is the deepest, and shows similar features to those seen by Heckman et al. (1987, 1990) and Keel (1990); a major result of the starburst-driven superwind is the hourglass oriented at a position angle 100° east of north. Throughout the text we refer to various bubbles and arms; for clarity we sketch them in Figure 3.

The $\text{H}\alpha + [\text{N II}]$ emission has been studied extensively by Yoshida et al. (2016), who found a network of bubbles and filaments extending 70×80 kpc, linked to three epochs of starburst-driven superwinds. In general, the $\text{H}\alpha + [\text{N II}]$ emission tracks the extended soft X-ray halo (Nardini et al. 2013), suggesting that these gas phases are linked. Max et al. (2005) compared the central $\text{H}\alpha + [\text{N II}]$ emission to H_2 emission and found qualitative similarities; this correlation confirms that the superwind is affecting gas of a wide range of densities. Indeed, most filamentary features in the H_2 emission have matching features in the CO(2–1) and the Fe XXV maps (the latter of which was pointed out in Wang et al. 2014). We examine the spatial structure of H_2 in the bubbles in Section 4.

Although the $\text{H}\alpha + [\text{N II}]$ emission has been well-studied, the complexity of the kinematic structure has prevented a detailed study of optical emission-line ratios in the Butterfly Nebula (e.g., Sharp & Bland-Hawthorn 2010). Our suite of optical and near-infrared emission-line maps is the most complete to date.

Most of the morphological differences between the various optical/NIR lines are driven in large part by dust attenuation. The blue lines $\text{H}\beta$ and $[\text{O III}]$ are heavily extinguished in the nucleus, and as we probe longer wavelengths, the nuclear region becomes much brighter. The most striking individual feature present is the intense, collimated $[\text{O III}]$ emission along the eastern arm. Although emission in other lines is present in that region, they do not peak along the same spatial line.

As noted in Wang et al. (2014), the Fe XXV emission matches the H_2 in overall morphology. To highlight the similarity, we reproduce several line maps from Figure 2 with contours overlaid. These maps shown in Figure 4 reinforce that where we detect H_2 emission; we see not only Fe XXV but also CO(2–1), particularly in extension to the southeast. Although some similarity may be only in projection, the presence of the same ~ 3 kpc loop to the southeast suggests that these regions likely represent structures containing truly multiphase gas: ranging from ~ 10 K to 7×10^7 K.

3.2. Emission-line Ratios

Emission-line maps are complex to interpret because they show a convolution of intrinsic gas properties like density and metallicity with extrinsic properties like the radiation field or shocks that are currently ionizing the gas. Further, dust extinction will affect how much of the flux emitted in each line reaches our telescopes, in a spatially-varying way. Some of these degeneracies can be limited by looking at emission line ratios. For example, pairs of emission lines close in wavelength will be affected by dust to a similar degree, and photoionization or shock models can predict the ratio of those two lines given particular gas properties and conditions. Line ratios are more exact than attempting to correct for extinction, which is challenging when different physical components (even along a single line of sight) are enshrouded by varying amounts of dust.

In Figure 5, we show the emission-line ratio maps constructed from the line maps described in Figure 2, smoothed by a median filter with a 3×3 pixel kernel to emphasize larger-scale structure, with two additions: the $\log([\text{N II}]/\text{H}\alpha)$ and the Balmer decrement $\text{H}\alpha/\text{H}\beta$ maps from our ground-based WiFeS integral field spectroscopy. We use the Balmer decrement from WiFeS here to show extinction instead of the HST-based $\text{Pa}\beta/\text{H}\beta$ ratio because the HST $\text{H}\beta$ image is not deep enough to probe the heavily extinguished nuclear regions.

The line ratio maps show several interesting features of the filamentary structure. The distributions of line ratios show a statistically significant excess of higher values in the filaments, compared to the diffuse and nuclear regions (Figure 6). Across the three optical line ratios probed, filamentary regions show a significant tail to higher ratios. A two-sided Kolmogorov–Smirnov test shows that the two samples are drawn from different populations to a strong significance ($p < 10^{-7}$).

We interpret these higher ratios as being due to shocks that are driven by the expansion of the bubbles. Note that these enhancements are underrepresented in the $[\text{S II}]$ and $[\text{O I}]$ panels because the same shocks also enhance the $[\text{N II}]$ emission, which is mixed in with $\text{H}\alpha$ here (see the Appendix and Figure 17 for pure line ratios at lower spatial resolutions). As suggested by the $[\text{O III}]$ map itself, the $[\text{O III}]/\text{H}\beta$ ratio map shows a sharp ridgeline in the eastern arm, likely pointing to a different ionization mechanism, which we explore below in Section 6.

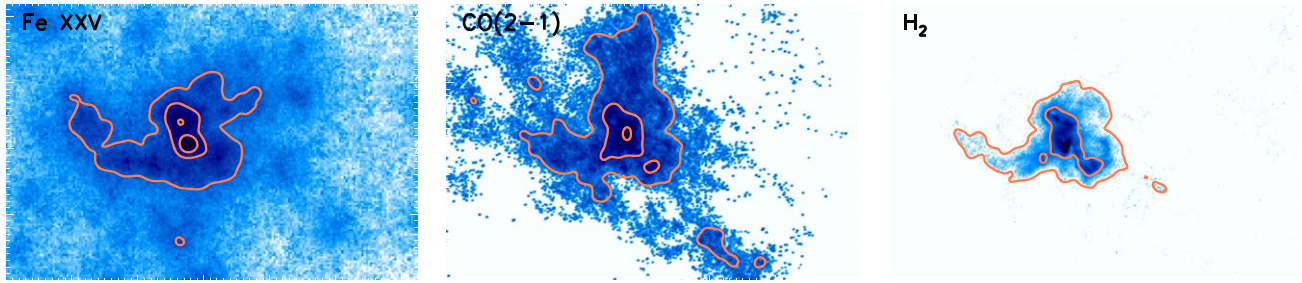


Figure 4. Maps of Fe XXV, CO(2–1), and H₂ emission as in Figure 2, but with individual contours overlaid in orange to highlight similar morphologies. All three emission lines are bright in the nuclei and extend north, southwest, and (most prominently) ~ 3 kpc to the southeast.

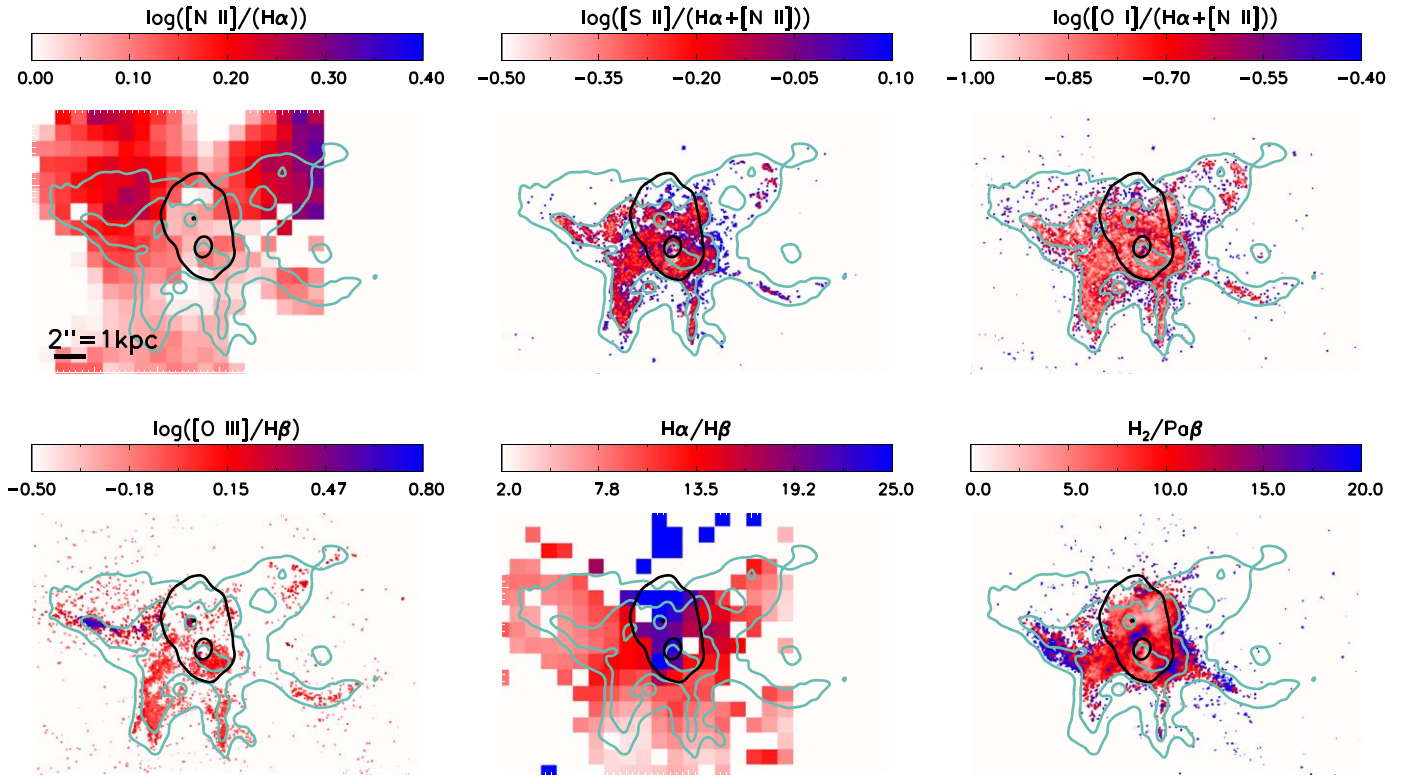


Figure 5. Maps of emission-line ratios (top row, left to right), $\log([N\text{ II}]/H\alpha)$ from WiFeS, $\log([S\text{ II}]/(H\alpha+[N\text{ II}]))$, $\log([O\text{ I}]/(H\alpha+[N\text{ II}]))$, and (bottom row, left to right) $\log([O\text{ III}]/H\beta)$, $H\alpha/H\beta$ from WiFeS, and H₂ 1–0 S(1)/Pa β . HST line maps are initially masked below 3σ and then median-filtered with a kernel of 3×3 pixels. Each panel has the $H\alpha+[N\text{ II}]$ contours (teal) and stellar continuum contours (black) from Figure 2 overlaid for comparison. The scale bar in the top left panel shows $2''.05$, approximately one kiloparsec.

We note that the H₂/Pa β ratios are consistently high, showing a large peak encompassing both nuclei (as identified by van der Werf et al. 1993, providing a strong argument for H₂ excited by merger-induced shocks) and enhancements along the filaments, similar to the optical line ratios. For reference, H₂/Br γ ratios in shock-excited gas tend to be $\gg 1$ (e.g., Puxley et al. 1990); using Case B recombination converts the threshold to H₂/Pa $\beta \gg 0.17$ (Hummer & Storey 1987), showing that shocks dominate the excitation of H₂ across the entire face of the galaxy. The widespread nature of shock-excited H₂ (elevated H₂/Pa β) is in contrast to the signatures of some outflows that produce shock-excited H₂ in distinct cones (e.g., in NGC 4945; Moorwood et al. 1996; Marconi et al. 2000; in M82; Veilleux et al. 2009; Beirão et al. 2015; in IRAS F08572 +3915; Rupke & Veilleux 2013; in IRAS F17207-0014; Medling et al. 2015; in IIIIZw035; U et al. 2019; although

among those cones, the structure varies). We examine the phase structure in the filaments of NGC 6240 in Section 4 and explore the dust structure and its relation to the molecular gas in Section 5.

3.2.1. Emission-line Diagnostics of Key Regions

To facilitate comparisons, we also examine line ratios in specific regions of interest. Figure 7 shows our selected regions overlaid on the $\log([O\text{ III}]/H\beta)$ and H₂ 1–0 S(1)/Pa β panels from Figure 5 for reference. For each region, we mask out spaxels below a 3σ detection limit and then compute the resistant mean using a further 3σ threshold. The narrowband [N II]+H α image was corrected based on the lower spatial resolution [N II]/H α ratio from our WiFeS data to obtain a (smoothed) pure H α image that we used to measure these line ratios.

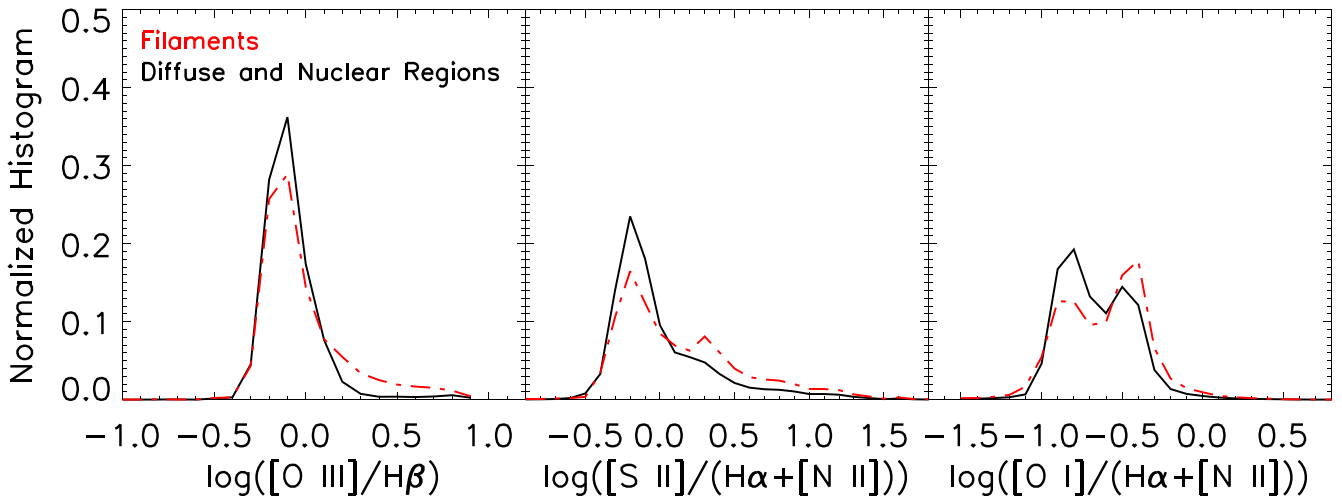


Figure 6. Normalized histograms showing the distribution of line ratios present in HST narrowband maps. In each panel, the red dotted-dashed line shows the distributions present along the filaments and edges of bubbles marked in Figure 3, and the black solid line shows the remaining spatial regions of the galaxy. In each panel, the filamentary regions have a tail toward higher line ratios. A K-S test confirms that the two distributions are drawn from different populations ($p < 10^{-7}$) in each case.

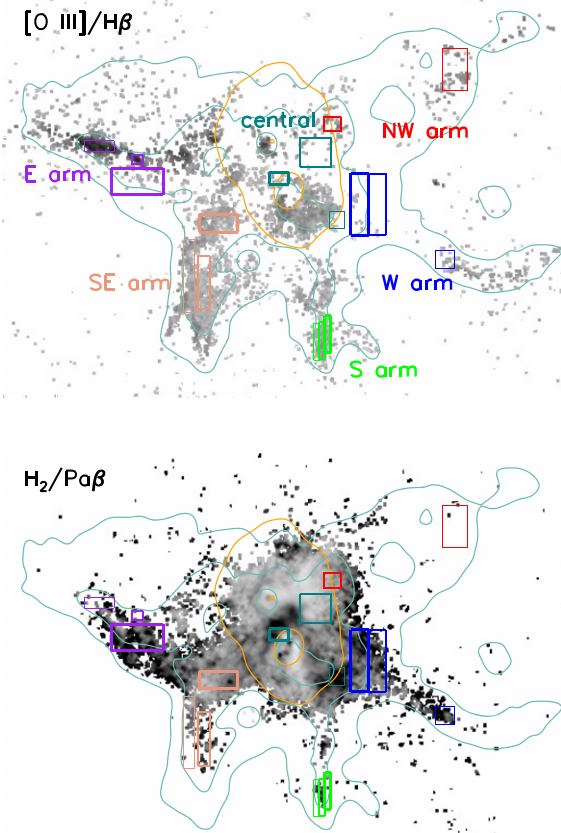


Figure 7. Maps of $\log([O \text{ III}]/H\beta)$ (top) and $H_2 1-0 S(1)/Pa\beta$ (bottom) from Figure 5 with selected regions of interest boxed for comparison. Line ratios within these regions are examined in Figure 8. The colors of the boxes here correspond to general areas of the galaxy, and match the colors in the diagnostic plots; within a color, the thinnest boxes correspond to the smallest symbols. Each panel also has the $H\alpha+[N \text{ II}]$ contours (teal) and stellar continuum contours (orange) from Figure 2 overlaid for reference.

As expected from Figure 5, the $[O \text{ III}]$ ridgeline in the eastern arm (smaller two purple diamonds in Figure 8) shows $[O \text{ III}]/H\beta$ ratios distinctly higher than all other points, leading them to stand out in most diagnostic plots. The enhanced $[O \text{ III}]/H\beta$ in

these two regions is almost but not quite sufficient to unambiguously place them in the AGN category. We note that shock-ionization and AGN-photoionization models overlap in this line ratio space, and further information is required to confirm the likely ionization mechanisms (which we explore in Section 6). The remaining regions are relatively tightly clustered in the LINER or shock-like ionization mechanism regime. It is interesting to note that the three central regions are among those that show the least AGN-like optical line ratios, demonstrating that the AGN are obscured from most of the surrounding ISM.

The selected regions also show a large spread (4x) in $H_2/Pa\beta$ ratio. In $[O \text{ III}]/H\beta$, a single arm was distinct from the other arms; with $H_2/Pa\beta$, each filament (color/symbol) also spans a range. We note that the outer regions of several arms show higher $H_2/Pa\beta$ ratios than other regions along the same arms. An enhanced line ratio may be indicating stronger or more dominant shocks or simply less star formation (lower $Pa\beta$ emission) along our line of sight farther from the nucleus (analogous to the increased optical line ratios in the outskirts of LIRGs; Rich et al. 2011). However, even the lowest ratios seen in our map ($H_2/Pa\beta \sim 2$) are about an order of magnitude above the typical ratios expected from UV-pumping associated with young star formation (Puxley et al. 1990; Doyon et al. 1994; Larkin et al. 1998; Davies et al. 2003).

We see no sign of correlation between $H_2/Pa\beta$ and each of $[N \text{ II}]/H\alpha$ or $[O \text{ III}]/H\beta$; a weak correlation may exist between $H_2/Pa\beta$ and each of $[O \text{ I}]/H\alpha$ and $[S \text{ II}]/H\alpha$, but it is not statistically significant (both have Pearson's correlation coefficients ~ 0.4). Such a correlation would not be unexpected because all three line ratios are shock tracers.

We also consider the effects of extinction on these shock diagnostics. By using ratios of lines close in wavelength, we expect that extinction itself does not heavily affect our direct measurements. However, the near-infrared light may be coming from physical regions more enshrouded by dust than the optical counterpart. If most shocked filaments were buried in dust, we would see a stronger shock signal in near-IR tracers than in optical tracers. In NGC 6240, we see evidence of shocked line ratios in both optical and near-IR tracers in all regions probed in Figure 7. We cannot rule out the possibility

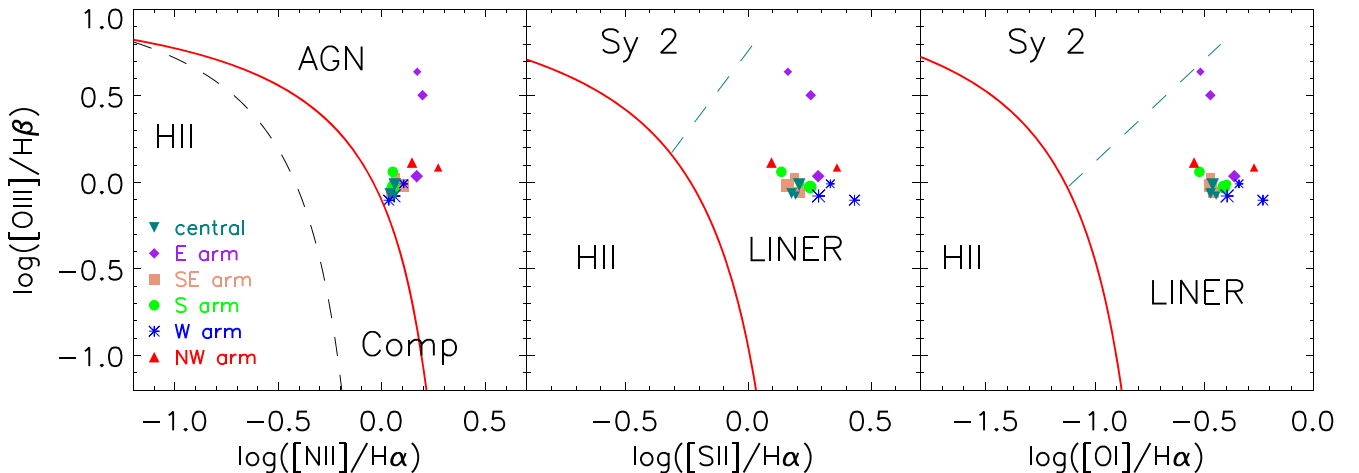


Figure 8. Diagnostic diagrams for regions described in Figure 7, following Baldwin et al. (1981) and Veilleux & Osterbrock (1987). Panels show (left to right) $\log([\text{O III}]/\text{H}\beta)$ vs. $\log([\text{N II}]/\text{H}\alpha)$, vs. $\log([\text{S II}]/\text{H}\alpha)$, and vs. $\log([\text{O I}]/\text{H}\alpha)$. We include the classification lines for different photoionization mechanisms from Kewley et al. (2006). Symbols are color-coded based on location in the galaxy: three central regions (teal downward-facing triangles), three from the eastern arm (purple diamonds), three from the southeastern arm (peach squares), three from the southern arm (green circles), three from the western arm (blue asterisks), and two from the northwestern arm (red upward-facing triangles). Each symbol is also size-coded to distinguish within a category: smallest symbols are farthest from the nucleus and have the thinnest lines in Figure 7. All regions are consistent with the shocks/LINER-like ionization mechanism except the two regions along the ridge of strong [O III], which are shifted toward AGN-like photoionization.

that some shocked gas is dust-enshrouded, but the presence of shocked optical line ratios tells us that some filaments are not completely obscured. Indeed, our Balmer decrement map (Figure 5) shows the most extreme extinction around the two nuclei (blue, $\text{H}\alpha/\text{H}\beta \sim 20$), and most filaments show lower Balmer decrements than the regions between them (e.g., E and SE arms are pale red with values < 10 , between them is bright red with values of 10–15).

4. Shock Structure in Bubbles

As a bubble of hot gas expands, it can shock the surrounding interstellar medium and create increased emission-line ratios along the edges (e.g., Weaver et al. 1977), exactly as we see here. As an example, we zoom in on the southeastern arm and examine the line maps in more detail (Figure 9). In this region, we propose that gas is outflowing from the nuclei (beyond the top right corner of each panel) in a southern or southeastern direction. The shock front would have expanded from the top right, moving across the panels until reaching its current location at the edge of the bubble. The [O III]/[O I] ratio probes the ionization structure directly: we see a significant enhancement of [O III] relative to [O I] along the outer edge of the shell, indicating the current location of the shock front. That is, the high ionization state of the gas here indicates that it is hotter and, therefore, more recently shocked than the gas to the west, which has had longer to cool.

Because [O I] at 6300 Å is significantly redder than the [O III] 5007 Å line, this ratio could be subject to variable dust extinction. However, if less dust extinction were causing the factor of 2–4 increase in the [O III]/[O I] ratio we see along the outer edge of the shell, the $\text{Pa}\beta/\text{H}\beta$ map should show a corresponding decrease by at least 30% in that region, which it does not.²⁴ Indeed, the [O III]/H β ratio is less subject to extinction and shows a similar increase along that shell. We note that this shell feature is unlikely to be an artifact of a

variable point-spread function across the relevant emission lines because the stars and star clusters used to register the different HST filters have statistically indistinguishable distributions of full width at half max. At a lower spatial resolution, the soft X-ray emission is spatially consistent with the edge of the bubble, although perhaps more aligned with the $\text{H}\alpha + [\text{N II}]$ contours than with the higher ionization [O III]/H β emission.

The small H α peak in the middle of the bubble highlighted in Figure 9 is likely a young star cluster located in front of the bubble. It shows higher $\text{Pa}\beta/\text{H}\beta$ ratios (~ 5) than the surrounding areas, suggesting it is still dust-enshrouded, and is colocated with a clump of cold molecular gas emitting CO(2–1). As with other star clusters, this clump shows no detected warm H $_2$; it may even be obscuring some warm H $_2$ emitted by the bubble behind it.

The presence of molecular gas in galactic winds (e.g., Sturm et al. 2011; Feruglio et al. 2013a, 2013b; Spoon et al. 2013; Veilleux et al. 2013; Cicone et al. 2014; González-Alfonso et al. 2017; Gowardhan et al. 2018) presents a theoretical challenge. We discuss three possible scenarios here:

1. *Molecular Gas Is Entrained:* Some high-resolution simulations of molecular clouds entrained in hot outflows suggest that the clouds might be quickly shredded and evaporate into the hot phase of the wind (Scannapieco & Brüggen 2015; Brüggen & Scannapieco 2016; Schneider & Robertson 2017). If molecular clouds are instead swept up and carried away by the outflowing gas, we expect the molecular gas to be evenly distributed across the face of an outflow. Depending on the density and size of the clouds, they would eventually evaporate into the wind and become less frequent farther from the launch of the outflow (Banda-Barragán et al. 2020). In this scenario, gas on the edges of each cloud may still be shocked even as the interior is shielded.
2. *Molecular Gas Is Dissociated and Reforms:* An alternative theory proposes that the shock front sweeps through and dissociates all molecular gas, after which the

²⁴ We do note that the decreased [O III]/[O I] near the top right of the panel is likely due to the increased dust extinction, traced by a higher $\text{Pa}\beta/\text{H}\beta$ ratio there.

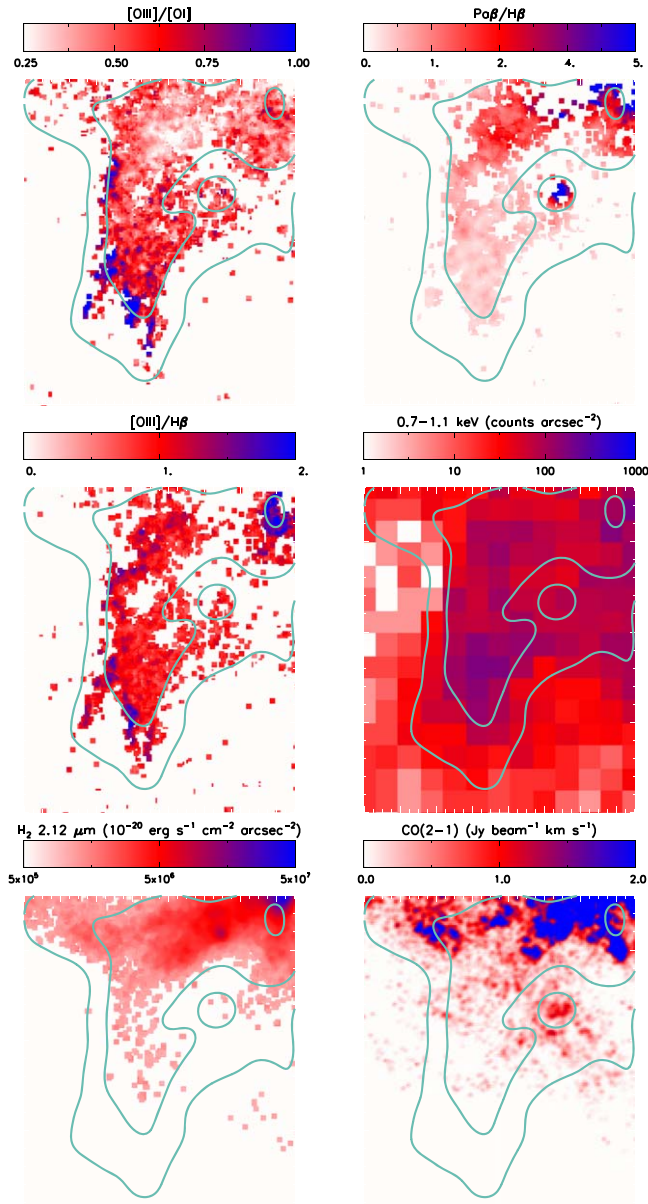


Figure 9. Zoomed-in region of the southeastern arm showing maps of [O III]/[O I] (top left), the Pa β /H β decrement (top right), [O III]/H β (center left), soft X-ray (center right), H $_2$ 2.12 μ m (bottom left), and CO(2–1) (bottom right). Teal contours show the H α +[N II] flux for comparison between panels. The [O III]/[O I] ratio is enhanced along the outer edge of the bubble (blue regions). The Pa β /H β ratio does not show a significant increase along the shell, so we are confident that the variation in [O III]/[O I] ratio is not due to variable dust extinction. This enhanced ionization is also shown in [O III]/H β and in the soft X-rays, confirming that the strongest shocks are present along the edge of the bubble. H $_2$ and CO emission are both present only in the interior of the bubble, and show no evidence for molecular gas reforming near the shock front.

initially hot winds cool adiabatically and/or radiatively as they expand until new molecular clouds form from remaining density fluctuations or behind the shock front (Thompson et al. 2016; Schneider et al. 2018) beyond a certain cooling radius. If the outflowing molecular gas is (re)formed, we might expect to see a higher incidence of molecular gas along the edges of a bubble. However, the location of this putative reformed molecular hydrogen depends on the cooling time/length, and could lag behind the shock front so far that we would not see its evidence

in this particular bubble. Ohyama et al. (2003) favored a similar scenario to describe the shocked H $_2$ emission between the two nuclei of NGC 6240, suggesting that an outflow from the southern nucleus shocks the already-existing molecular gas bridge between the nuclei, crushing molecular clouds along the shock front. We note that this scenario suggests that the lack of molecular gas in the middle of the bubbles is purely due to the shock having dissociated it; consequently, you should expect molecular gas *outside* the shock front, on the left edge of these panels.

3. *Molecular Gas Is Avoided:* The simulations of Wagner et al. (2013) show a third possibility: that the hot outflow mostly avoids the dense, clumpy molecular clouds, forging pathways around them. In this scenario, the distribution of the molecular gas is mostly unchanged from a pre-outflow scenario: that is, likely higher density closer to the nuclei (as we see). The fact that the shock front is visible outside of the region containing molecular gas demonstrates that the hot wind was able to find pathways between the molecular gas and continues to push aside the remaining ISM. As with the first scenario, the gas on the edges of each cloud may still be shocked, producing signatures such as warm H $_2$ 2.12 μ m emission and high H $_2$ /Pa β ratios.

In Figure 9, the CO(2–1) and H $_2$ emission fade quickly with distance from the nuclei and are here detected solely interior to the shocked shell of the bubble traced by the enhanced [O III]/H β and [O III]/[O I] ratios. The lack of CO(2–1) or H $_2$ emission beyond the shock front traced by high [O III]/[O I] (i.e., on the left edge of the panel) suggests against the second scenario. We argue then that the molecular gas seen inside the bubble is not gas that has been dissociated-and-then-reformed. Still, if the cooling time/length were as short as it is in some other merging systems ($\sim 10^5$ yr, \sim few hundred pc in Stephan’s Quintet; Guillard et al. 2009), it ought to be possible here if gas densities are high enough. We note that some other filaments of H $_2$ (e.g., the western arm, between the nuclei, and below the eastern arm) show increased H $_2$ /Pa β ratios. It is possible that conditions are different enough there to enable molecules to reform below or behind a shock front, or that something else is going on entirely, like the collision of two spiral arms along our line of sight. Further, it is possible that the shock front was responsible for dissociating molecular gas previously, when the shock front had not yet expanded beyond the molecular-gas-rich nuclear region, but now is no longer overtaking substantial amounts of molecular gas.

Our data cannot distinguish between the first and third scenarios. Both scenarios predict that the molecular gas decreases in density along the length of the outflow, can be present inside the bubble, would exhibit some warm H $_2$ emission, and need not be present outside the shock front. Future analysis comparing the kinematics of CO(2–1), warm H $_2$, and ionized gas emission lines are needed to determine how/if the molecular gas is moving along with the outflow.

5. The Spatial Structure of Molecular Gas and Dust

Most of the molecular gas traced by CO is in a ribbon or bridge between the two nuclei (Tacconi et al. 1999), although significant CO(2–1) emission is seen extending $\sim 6''.5$ (> 3 kpc) from the nuclei in several directions. Our narrowband

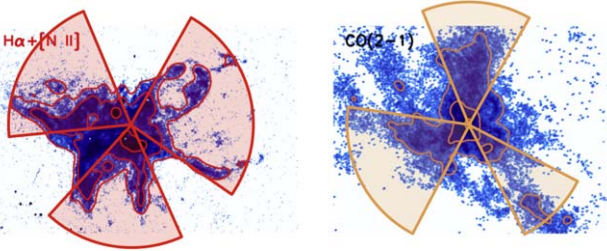


Figure 10. $\text{H}\alpha$ (left) and $\text{CO}(2-1)$ (right) emission-line maps from Figure 2, reproduced with their flux contours in red and orange, respectively. In each panel, we overlay wedges extending from the nucleus along the regions of increased ionized or molecular gas, to highlight that the two phases of gas are qualitatively anticorrelated. Such an anticorrelation may indicate that the hot ionized gas is flowing outwards along the path of least resistance, in between clumps of the denser molecular gas.

H_2 emission also traces this bridge, similar filamentary structure within the central kiloparsec, and the extended arm to the southeast. We detect no warm H_2 component in the northern or southern-southwestern CO extensions. Interestingly, we do see warm H_2 in the southwestern arm and farther along the eastern arm that appears to have only a much weaker CO counterpart.

Feedback in a galaxy with a multiphase ISM involves the hot gas expanding outwards, symmetrically, until it reaches something to block it. Dense clumps of molecular gas are harder to accelerate, so the gas may expand around them, following a path of least resistance (e.g., Wagner et al. 2013), just as in the third scenario of Section 4. The molecular gas structure here is reminiscent of that scenario: extended/clumps of CO(2–1) to the north, southeast, and southwest all align well with spaces *between* the bubbles traced by ionized gas filaments (at least in projection; of course the three-dimensional structure may be more complex). We highlight the spatial anticorrelation between $\text{H}\alpha$ and $\text{CO}(2-1)$ emission in Figure 10.

Our Balmer decrement map, shown in Figure 5, demonstrates that the bulk of the dust extinction also appears around or between the nuclei, with moderate increases toward the southeastern and southwestern arms, spatially coincident with the CO(2–1) emission and, particularly, its northern extension. We note that the actual extinction could be higher in places because we are only tracing the regions where $\text{H}\alpha$ and $\text{H}\beta$ are optically thin. The presence of dust may be necessary to shield the H_2 from dissociation, or we may simply be seeing evidence of a constant gas-to-dust-mass ratio, wherein the denser regions of gas happen to also host more dust mass.

We calculate the mass present in warm H_2 from the H_2 2.12 μm emission-line following Veilleux et al. (2009). Assuming the H_2 molecules are thermalized at $T = 2000 \text{ K}$, $M_{\text{H}_2} = 0.00133 [L_{S(1)}/L_\odot] M_\odot$. For comparison, we also calculate the mass of cold H_2 traced by our CO map using the mean $\alpha_{\text{CO}} = 2.5$ and $r_{21} = 1.17$ measured across NGC 6240 by Cicone et al. (2018). The resulting maps (Figure 11) show that, in the large ribbon of molecular gas between the nuclei, only a small fraction ($\sim 3 \times 10^{-6}$) is excited by shocks or ultraviolet photons; however, in the filaments, the fraction is roughly 100 times higher. For comparison, the outflow in M82 shows an integrated warm/cold (from H_2 2.12 μm relative to CO(2–1)) gas mass ratio of 3×10^{-5} (Walter et al. 2002; Veilleux et al. 2009), an intermediate value in the range we see here. We also estimate the rough fraction of warm-to-cool gas

expected in a pure star-forming region as follows: the Orion Nebula has an $\text{H}_2/\text{Br}\gamma$ ratio of $10^{-1.2}$; we convert the H_2 to mass as above, and convert the $\text{Br}\gamma$ luminosity to a star formation rate and the star formation rate (in unit surface area) to a gas mass (in the same unit surface area) following relations in Kennicutt (1998). Thus, we estimate the mass fraction traced by H_2 2.12 μm to that traced by CO(2–1) as roughly 10^{-6} in a pure star-forming system. As an independent constraint, we extrapolate from the warm H_2 fractions of galaxies from the Spitzer Infrared Nearby Galaxies Survey (SINGS; Roussel et al. 2007 and their Figure 7, top left panel). When defining *warm* H_2 as the $T > 2000 \text{ K}$ gas traced by our 2.12 μm transition, a pure star-forming region should have a warm-to-cold H_2 fraction of $\sim 2.5 \times 10^{-6}$. Both estimates of warm-to-cold H_2 fractions in normal star-forming regions are below most of the map in the bottom left panel of Figure 11.

The sometimes substantial extinction can affect these ratio maps, as follows. In regions with high extinction (i.e., around the nuclei and extending north), the H_2 2.12 μm emission will be more attenuated than the longer-wavelength CO(2–1), artificially depressing the warm to cold gas mass ratio maps. Further, the H_2 2.12 μm emission will be less attenuated than the $\text{Pa}\beta$ emission at shorter wavelengths, potentially inflating the subsequent line ratio map. Our Balmer decrement map from Figure 5 suggests A_V ranges from ~ 1 to > 100 with a strong spatial dependence. Because we only have a measure of high extinction at a low spatial resolution, we do not apply a direct correction to these maps, and note that the warm to cold gas ratio measured here is likely an underestimate.

We also note that the fraction of warm-to-cold molecular gas depends heavily on the definition of warm and, thus, on the observed transitions of H_2 emission; mid-infrared lines will trace the cooler gas (100–500 K) that represent a larger mass of shocked gas (see e.g., M82 in Beirão et al. 2015). Future analyses mapping both near- and mid-IR transitions of H_2 at comparable spatial resolutions will be possible with the James Webb Space Telescope (JWST) in the coming years and (along with ALMA dense gas mapping) will reveal the temperature and shock structure of the molecular gas.

The strong 2.12 μm emission along the ribbon between the nuclei has been attributed to intense shocks due to the ongoing collision of the two nuclei (e.g., Tecza et al. 2000), and the region's high CO line-to-continuum ratio may require strong shocks (Meijerink et al. 2013). Interestingly, we see no increase in the fraction of molecular gas that is shock-excited in this region between the nuclei. Ohyama et al. (2003) also found an increase in 2.12 μm production efficiency moving away from the nuclei (primarily toward the southwest). The spatial variation in the fraction of excited H_2 is qualitatively similar to the $\text{H}_2/\text{Pa}\beta$ map also shown in Figure 11, where the ratio is higher farther from the nucleus, with the notable exception of a very high $\text{H}_2/\text{Pa}\beta$ ratio in the bridge between the nuclei. The molecular gas in the bridge, therefore, is not necessarily too warm to form stars, but star formation is nonetheless suppressed, perhaps by turbulence. A full analysis of the CO kinematics at these spatial resolutions will be presented in a forthcoming paper. The increasing fraction of shock-heated molecular gas farther from the nucleus has been seen frequently in optical shock studies, and is usually interpreted as the star formation decreasing rather than shocked gas increasing (e.g., Rich et al. 2011). Our comparison of warm to cold molecular gas may provide a more direct measure of the spatially-varying

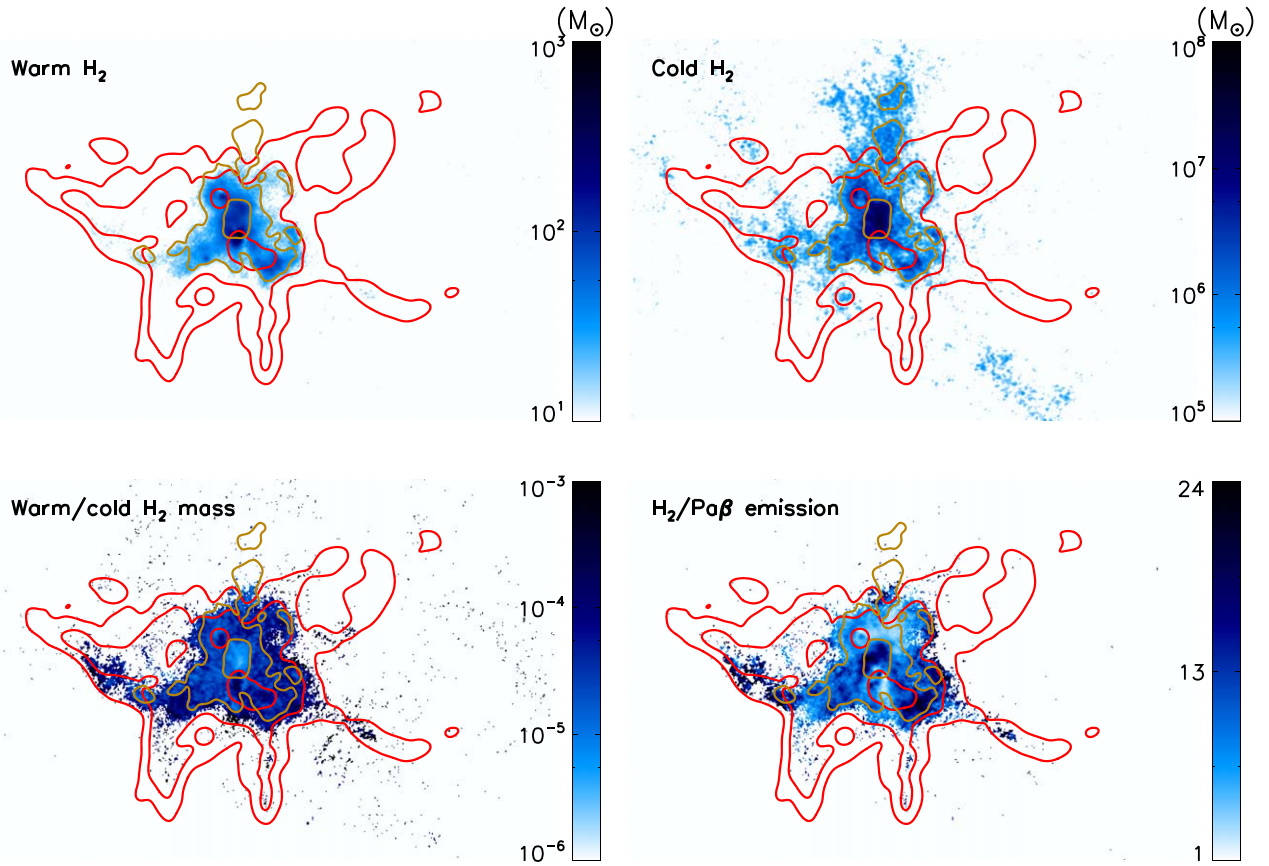


Figure 11. Top: mass maps (in M_{\odot} pixel $^{-1}$) of warm ($T \sim 2000$ K) H_2 calculated from the H_2 2.12 μm emission and of cold H_2 calculated from the CO(2–1) emission. Bottom: $H_2/CO(2-1)$ and $H_2/\text{Pa}\beta$ ratio maps with $H\alpha+[N\text{ II}]$ (red) and CO(2–1) (gold) contours for comparison. The mass fraction of warm molecular gas increases to $\sim 10^{-4}$ in the filaments, 1–2 orders of magnitude larger than in the shocked bridge between the nuclei.

state of the gas, and confirms that shocks are more dominant in the filaments.

6. Collimated [O III] Emission

The two regions from Figures 7 and 8 that fall along the collimated [O III] emission show high $\log([O\text{ III}]/H\beta)$ ratios (>0.5) but are unremarkable in all other emission-line ratios we considered. These high $\log([O\text{ III}]/H\beta)$ ratios suggest that gas along this region is ionized by a different mechanism than the other filaments present in this galaxy. Müller-Sánchez et al. (2018) identified this [O III] emission as the edge of an ionization cone. The western arm is aligned with our ridgeline on the opposite side of the nuclei; it may be a counterpart to the ionization structure, although the [O III]/H β and other line ratios are more consistent with the other filaments than with the eastern arm. The southeastern extension of molecular gas loops north, becoming more shocked as it approaches the ridgeline of high $\log([O\text{ III}]/H\beta)$, although it does not extend far enough to overlap. We see two possible scenarios explaining the ridge-line: either this region shows a collimated jet from one of the AGN shock-heating the gas or a direct line-of-sight path has enabled this gas to be photoionized from the AGN’s radiation field.

In either case, the energy source is likely one or both of the two AGN. The length of the [O III] ridge points directly to the southern nucleus. Indeed, the projected line of sight aligns with the axis of rotation of the nuclear disk surrounding the southern AGN (Medling et al. 2011, 2014), with only a small offset

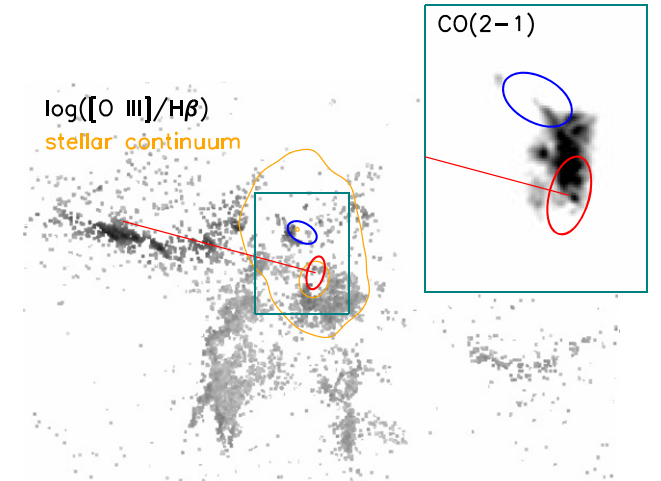


Figure 12. Schematics of northern (blue) and southern (red) nuclear disks modeled in Medling et al. (2014) overlaid on $\log([O\text{ III}]/H\beta)$ map. Axis ratios and position angles are as fitted, but sizes are enlarged for clarity. Red line shows projected minor axis of southern disk, closely aligned with the high [O III]/H β ridgeline. Stellar continuum contours are shown in orange. The inset shows a zoom-in of the teal box with gray scale of CO(2–1) emission and schematics overlaid, highlighting the possible ring structure along the line between the southern nucleus and the high [O III]/H β ridgeline.

(Figure 12). A small ringlike structure in the CO(2–1) is visible just east of the southern nucleus, along its minor axis, along the projected path to the eastern arm. Although the high

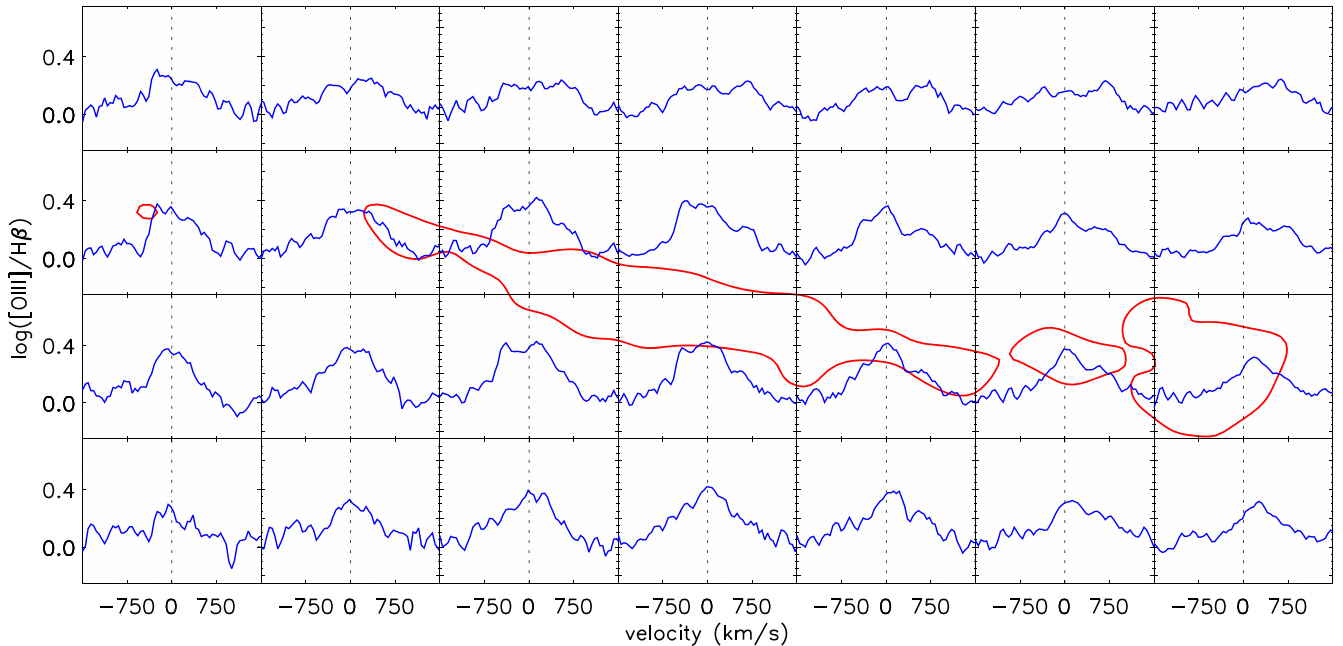


Figure 13. $\log([O\ III]/H\beta)$ ratios as a function of velocity for the $7'' \times 4''$ region around the ridge taken from our WiFeS integral field spectroscopy, with each panel corresponding to an individual WiFeS spaxel. The emission-line ratios have been smoothed over three spectral channels to better show the velocity structure. For comparison, contours from the HST-derived $\log([O\ III]/H\beta)$ map in Figure 5, covering the same spatial region, are shown in red. Note that seeing will smear out the signatures of the ridge over multiple WiFeS spaxels. Across the whole spatial region, the $[O\ III]/H\beta$ ratios show a similar kinematic structure: centered around systemic velocity; lines are broad (several hundred km s^{-1} everywhere). The high $[O\ III]/H\beta$ gas does not show the velocity gradient or strong velocity offset that would be expected from an outflow (unless it is in the plane of the sky).

$\log([O\ III]/H\beta)$ ridgeline extends almost due east from the northern AGN, the position angle of that nuclear disk points S-SE, so an AGN-driven jet or beam of radiation would have to emerge closer to the plane of the disk.

In Figure 13, we show the line profiles from our WiFeS integral field spectroscopy for a $7'' \times 4''$ region around the ridge. The red contours in the background show the spatial region over which the high $[O\ III]/H\beta$ ridge would contribute if beam smearing were not an issue. In these data, however, the $1''.5$ seeing has smeared out the spectral signatures of the ridge over most spaxels in the given region. These spectra show only minor differences between the kinematic structures of $[O\ III]$ and $H\beta$. The minor enhancement in $[O\ III]$ over $H\beta$ in spaxels dominated by the ridgeline is centered at systemic velocity. The lack of a strong velocity offset of the high $[O\ III]/H\beta$ gas argues against the AGN-driven outflow interpretation; although if the outflow is mostly in the plane of the sky, its velocity offset would be hard to detect. The broad nature of both $[O\ III]$ and $H\beta$ are consistent with a highly turbulent outflow, but also could be due to beam smearing of a complex kinematic structure; the multi-peaked nature of the individual line profiles suggests the latter.

If the $[O\ III]$ arm traces out a collimated jet or other outflow signature, we would expect evidence of shocks across all tracers. However, we see no evidence of enhanced $[S\ II]/H\alpha$, $[O\ I]/H\alpha$, $H_2/\text{Pa}\beta$, Fe XXV, or soft X-rays along this ridgeline in our maps, and the two regions standing out so highly in $[O\ III]/H\beta$ in Figure 8 are not elevated in other line ratios. Shocked gas often displays a positive correlation between line ratio and velocity dispersion (e.g., Rich et al. 2011; D’Agostino et al. 2019; Kewley et al. 2019), which we see across the entirety of NGC 6240 in Figure 14. However, the spaxels along the $[O\ III]$ ridgeline do not show such a correlation, further

arguing that its ionization is not shock-dominated. We also consider the possibility that some excess ionization is due to a fully ionized shock precursor here that is not present elsewhere in the galaxy. Sutherland & Dopita (2017) find that shock precursors transition to fully ionized around shock velocities of $>140 \text{ km s}^{-1}$, but we see no evidence that the $[O\ III]$ emission has a stronger velocity offset (Figure 13) or broader velocity dispersions (Figure 14) than the shocks present across the majority of the galaxy. However, we note that velocity dispersions across the galaxy, if they are due to shocks, are easily capable of photoionizing precursor gas everywhere. We cannot rule out the possibility that the E arm ridgeline represents a unique location where we get the best view of said precursor gas radiating, although we also see no particular evidence to support it (i.e., higher gas densities).

If the putative jet were strong enough to drill through the ISM without stirring it up, we would expect to see evidence in the radio, but no radio emission is evident along the eastern arm (Colbert et al. 1994), although a relic radio feature suggests a jet may once have pointed in this direction (Yun et al. 1999). On the other hand, if we were looking at beam of ionizing radiation from an AGN, we would expect the ionization parameter to decrease with the radius unless the density also decreases. We do not see a trend in $[O\ III]/H\beta$ along the $\sim 300 \text{ pc}$ of the ridgeline, although we also do not have a measurement for the density of hydrogen along the same spatial scales. (We note that the molecular gas mass surface density from our CO(2–1) emission does not show a significant trend along the ridgeline.)

We summarize the evidence in support of each scenario in Table 2. Although not conclusive, we find the evidence more in favor of a beam of AGN photoionization causing the enhanced $[O\ III]/H\beta$ in the eastern arm.

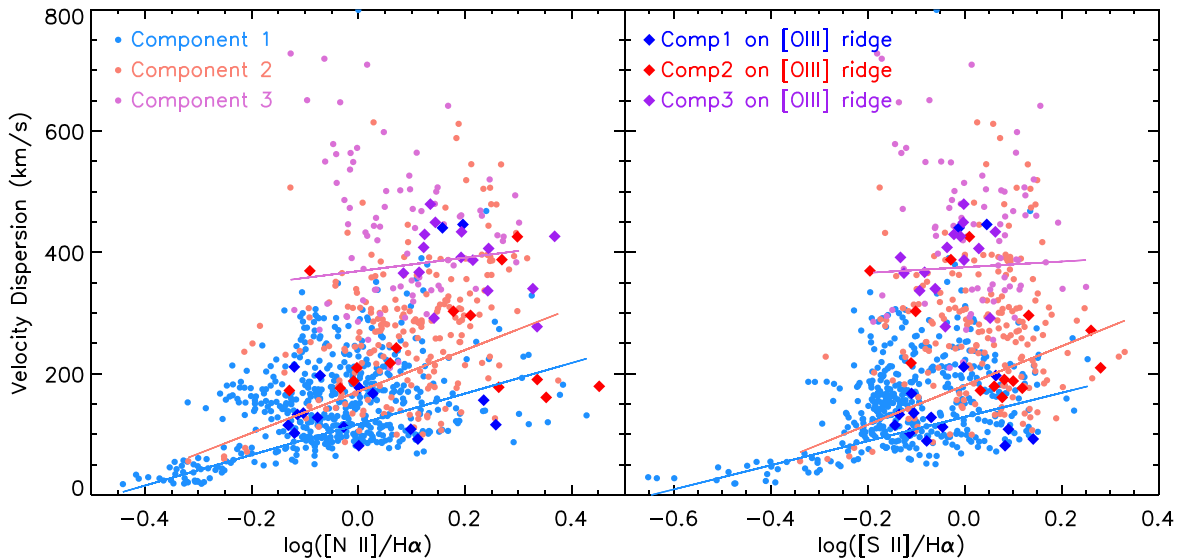


Figure 14. Velocity dispersion as a function of $\log([N\text{ II}]/H\alpha)$ (left) and $\log([S\text{ II}]/H\alpha)$ (right) ratios for each of the three Gaussian components (sorted from narrow to broad) fit for all spaxels from the WiFeS data meeting a signal-to-noise ratio of 5 or higher in relevant emission lines. Bold-colored larger diamonds represent spaxels appearing along the $[O\text{ III}]$ ridgeline. Overall, the two narrower components in each spaxel show statistically significant positive trends for both line ratios, a key signature of shocks, while the broadest component does not. The spaxels lying along the high $[O\text{ III}]$ ridgeline show no positive trends in any component.

Table 2
[O III] Arm Evidence

Evidence	Y/N
Scenario I: Collimated AGN Jet or Outflow	
Elevated $[O\text{ III}]/H\beta$	Y
Aligns with a nucleus	Y
Optical line ratios consistent with shocks	Y
Optical line ratios correlated with velocity dispersion	N
Elevated H_2 2.12 μm , Fe XXV, soft X-ray emission	N
Radio emission tracing the jet/ridge	N
Enhanced optical line widths	N
Scenario II: AGN Photoionization through a Keyhole	
Elevated $[O\text{ III}]/H\beta$	Y
Aligns with a nucleus	Y
Optical line ratios consistent with AGN — or consistent with AGN + shock mixing	some Y
Optical line ratios uncorrelated with velocity dispersion	Y
Unremarkable optical line widths	Y
Decreasing $[O\text{ III}]/H\beta$ with AGN distance (if constant n_e)	N

7. Conclusions

We present high spatial resolution emission-line maps from the Hubble Space Telescope, ALMA, and the Keck Observatory, and optical integral field spectroscopy from the Wide-Field Spectrograph of the Butterfly Nebula of NGC 6240. Our data set enables a detailed comparison of the multiphase energetics in and around the filaments and bubbles associated with starburst- and AGN-driven winds. We find:

1. The bubbles inflated by the superwind expand outwards along the paths of least resistance, avoiding regions with the highest densities of molecular gas.
2. Shocked molecular gas is seen along most but not all filaments and is generally interior to the outer shock fronts traced by optical ionization line ratios. This morphology suggests that either molecular gas is

entrained in the outflows and evaporates within a few kiloparsecs, or that it is not entrained at all. We do not see evidence for molecular clouds being dissociated and then reforming behind shock fronts, although we do note that the phase structure varies between filaments.

3. We find a ratio of warm H_2 ($T \sim 2000$ K, traced by the 1–0 S(1) transition at 2.12 μm) to cool H_2 (traced by the CO(2–1) transition) of $\sim 5 \times 10^{-6}$ by mass between and around the nuclei, with no obvious increase in shock-excited gas in the ribbon between the two nuclei. However, toward the edges of the nuclear region and along the filaments, the fraction does increase to roughly 10^{-4} . Cloud-crushing in the bridge associated with the two nuclei merging is, therefore, not a significant cause of shock-excitation in NGC 6240 compared to outflows.
4. A narrow ridge of elevated $[O\text{ III}]/H\beta$ emission in the eastern arm aligns spatially with the minor axis of the southern nucleus' disk. This emission is likely either a tightly collimated outflow from the AGN or a pencil-beam of radiation that found a path through the otherwise thickly obscuring interstellar medium. The highly ionized gas shows none of the kinematic signatures of an outflow, favoring the latter scenario.

We would like to thank many for helpful discussions related to the interpretation of this rich data set, including Phil Appleton, Bruce Draine, Rosalie McGurk, Patrick Ogle, Rick Pogge, and Ralph Sutherland, and Emanuele Nardini and Junfeng Wang for sharing their processed X-ray maps. We also thank the referee for careful readings and, especially, the scientific editor for patience while pandemic situations delayed our responses.

The authors wish to recognize and acknowledge the very significant cultural role and reverence that the summit of Maunakea has always had within the indigenous Hawaiian community; we are privileged to be guests on your sacred mountain. We wish to pay respect to the Gamilaraay/Kamaroi language group Elders—past, present, and future—of the traditional lands on which the Siding Spring Observatory

stands and to the Atacameño community of the Chajnantor Plateau, whose traditional home now also includes the ALMA observatory.

Support for A.M.M. was provided in part by NASA through Hubble Fellowship grant #HST-HF2-51377 awarded by the Space Telescope Science Institute, which is operated by the Association of Universities for Research in Astronomy, Inc., for NASA, under contract NASS-26555, and in part from the National Science Foundation under grant No. 2009416. A.M. M. and L.J.K. acknowledge the support of the Australian Research Council (ARC) through the Discovery project DP130103925. Parts of this research were supported by the Australian Research Council Centre of Excellence for All Sky Astrophysics in 3 Dimensions (ASTRO 3D), through project number CE170100013. C.E.M. acknowledges support by the National Science Foundation under award number AST-0908796. K.L.L. is supported by NASA through grants HST-GO-13690.002-A and HST-GO-15241.002-A from the Space Telescope Science Institute, which is operated by the Association of Universities for Research in Astronomy, Inc., under NASA contract NASS-26555. T.D.-S. acknowledges support from ALMA-CONICYT project 31130005 and FONDECYT regular project 1151239. E.T. acknowledges support from CATA-Basal AFB-170002, FONDECYT Regular grant 1190818, ANID Anillo ACT172033, and Millennium Nucleus NCN19_058 (TITANS).

This research is based on observations made with the NASA/ESA Hubble Space Telescope obtained from the Space Telescope Science Institute, which is operated by the Association of Universities for Research in Astronomy, Inc., under NASA contract NAS 5-26555. These observations are associated with programs 12552, 13690, and 10592.

Some of the data presented herein were obtained at the W. M. Keck Observatory, which is operated as a scientific partnership among the California Institute of Technology, the University of California, and the National Aeronautics and Space Administration. The Observatory was made possible by the generous financial support of the W. M. Keck Foundation. We enthusiastically thank the staff of the W. M. Keck Observatory and its AO team for their dedication and hard work.

This paper makes use of the following ALMA data: ADS/JAO.ALMA#2015.1.00370.S and ADS/JAO.ALMA#2015.1.00003. S. ALMA is a partnership of ESO (representing its member states), NSF (USA), and NINS (Japan), together with the National Research Council Canada, the Academia Sinica Institute of Astronomy and Astrophysics (Taiwan), and the Korea Astronomy and Space Science Institute (Republic of Korea), in cooperation with the Republic of Chile. The Joint ALMA Observatory is operated by ESO, Associated University, Inc./NRAO, and the National Astronomical Observatory of Japan. The National Radio Astronomy Observatory is a facility of the National Science Foundation operated under cooperative agreement by Associated Universities, Inc.

Facilities: HST (ACS and WFC3), ATT (WiFeS), Keck:II (Laser Guide Star Adaptive Optics, OSIRIS, and NIRC2), ALMA, and CXO (ACIS).

Software: LZIFU (v1.1; Ho et al. 2016) and PyWiFeS (v0.6.0; Childress et al. 2014).

Appendix

Seeing-limited Emission-line Maps from the WiFeS Data Set

Selected analysis products from our WiFeS integral field spectroscopy have been presented in the main body of the paper. For completeness and for comparison with the higher spatial resolution emission-line maps from narrowband imaging above, we present all the remaining WiFeS emission-line flux maps here, as well as some further analysis.

Using LZIFU (Ho et al. 2016), we fit up to three Gaussian components to each emission line; statistical F-tests show that all are justified (and perhaps even more) in most of the spaxels. However, at these limited spatial resolutions, a galaxy as complex as NGC 6240 has many overlapping physical components that are smeared out: two nuclei as well as numerous filaments, bubbles, outflows, clusters, tidal tails, and streams. As such, we caution the reader against too much interpretation of these data and do not present kinematic maps of the individual components.

In Figure 16, we show the emission-line flux maps. Because many of the spectral profiles are so complex that even three Gaussian components may not accurately describe them, we hesitate to attribute pure physical meaning to any individual component. Therefore, we show the sums of the three Gaussians for each line for each spaxel. Even so, we favor the parametrized framework in order to do the best job deblending the H α and [N II] lines. We note that the high spectral resolution of the WiFeS red arm ($R \sim 7000$) is capable of deblending the H α and [N II] lines easily in a normal system, but the complex kinematics and broad components of the lines pose a challenge that spectral resolution cannot solve (Figure 15). IFS with improved spatial resolution may provide some opportunity to spatially separate the complex kinematic structures into more distinct line profiles in the future.

We also show the key diagnostic line ratio maps [N II]/H α , [S II]/H α , [O I]/H α , and [O III]/H β in Figure 17 following Figure 5. Although these maps are at significantly lower spatial resolution than those constructed from the HST narrowband images, they have an important feature: we are able to spectrally separate H α and [N II], so the line ratios are purely forbidden transitions to recombination lines. The HST images constructed from [S II]/(H α +[N II]) and [O I]/(H α +[N II]) show much less

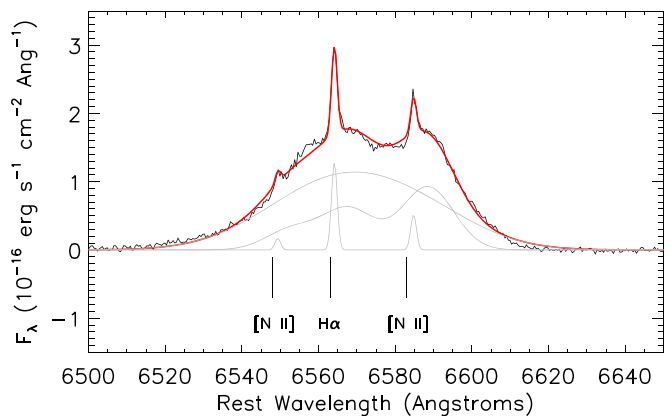


Figure 15. Example continuum-subtracted red-arm spectrum from our WiFeS data of a single 1'' \times 1'' spaxel near the nuclei, zoomed in on the H α -[N II] complex to demonstrate the challenging kinematic blending. We show in gray the LZIFU-fit three individual kinematic components for each line and the sum of all line components in red.

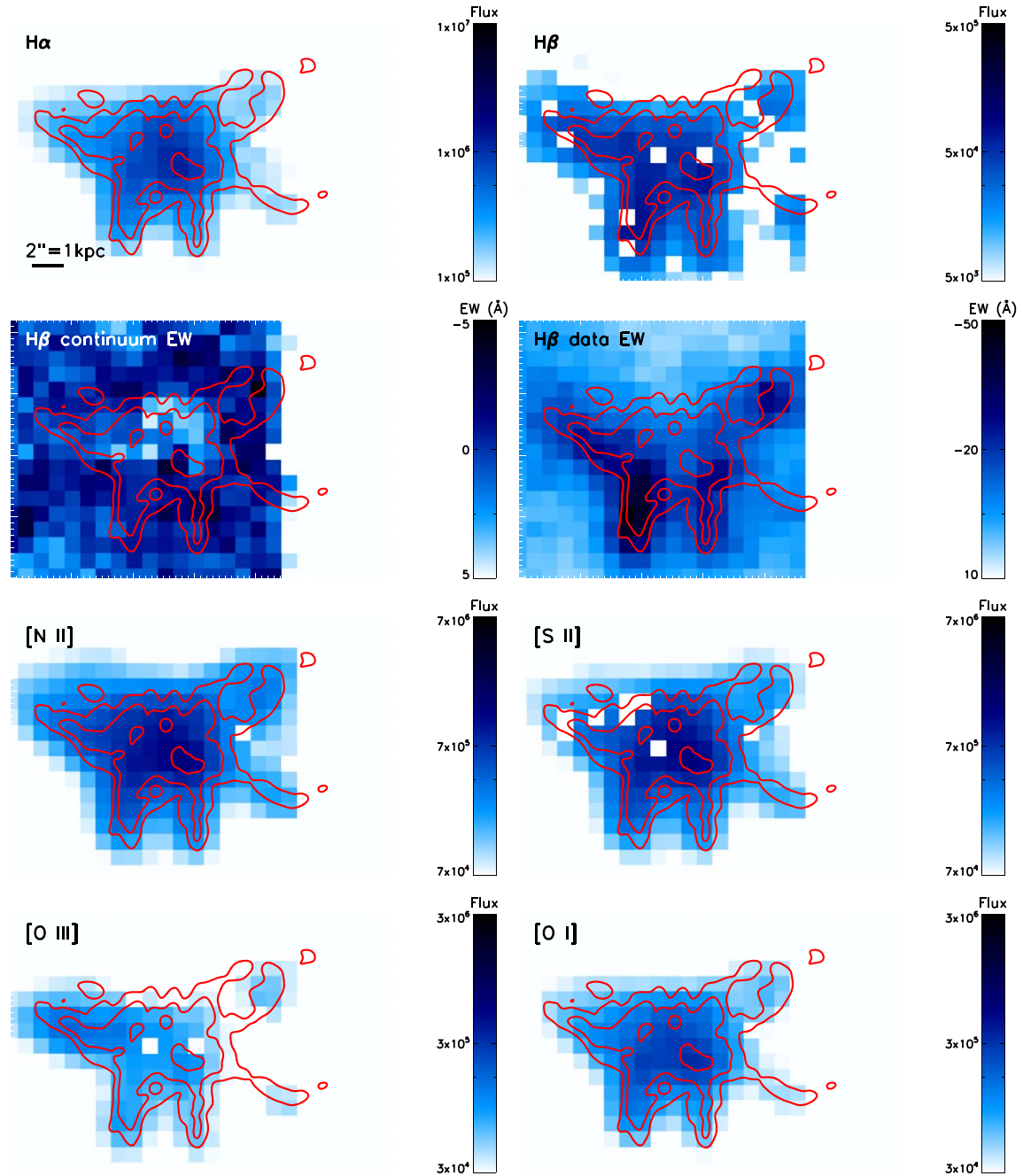


Figure 16. Maps of emission lines H α , H β , [N II], [S II], [O III], and [O I] from WiFeS seeing-limited integral field spectroscopy. Each panel is shown in log scale with limits chosen to emphasize structure, and has the HST H α +[N II] contours (red) overlaid for comparison. Line emission flux maps are shown in units of 10^{-20} erg s $^{-1}$ cm $^{-2}$ arcsec $^{-2}$. The second row shows the equivalent widths of H β in the continuum fit (left) and for the overall datacube (right), to illustrate the effects of Balmer absorption on the HST narrowband images: up to 30% in the nuclei and minor in the outer arms. A negative EW (darker colors) represents emission and positive EW (lighter colors) absorption. The scale bar in the top left panel shows $2''.05$, approximately one kiloparsec. Spaxels for which the emission-line fit failed or for which the S/N < 3 are masked in white.

enhancement along the filaments than the pure line ratios [S II]/H α and [O I]/H α probed by our WiFeS data. This effect is due to a cospatial enhancement of [N II] along the same filaments. The [O III]/H β map also shows an enhanced line ratio along the eastern arm, but the lower spatial resolution washes it out considerably. The most surprising feature revealed from the WiFeS data is the variation between the [N II]/H α and [S II]/H α ratio maps; in particular, [N II] is enhanced to the northeast and northwest of the Butterfly Nebula. Indeed, diffuse [N II] and H α extend in our WiFeS data $\gtrsim 5$ kpc north of the upper edge of the

panels in Figures 16 and 17, as was also seen in the narrowband images of Veilleux et al. (2003). This diffuse emission is detected at low significance in our HST F673N and F680N images; the detections are below our 3σ cutoff and are, therefore, masked out. However, extended diffuse [S II] is either considerably weaker or undetected even in our WiFeS data set.

In Figure 18, we translate the line ratio maps from Figure 17 into the optical emission-line diagnostic diagrams from Baldwin et al. (1981) and Veilleux & Osterbrock (1987). The spectra across the field of view show elevated line ratios mostly

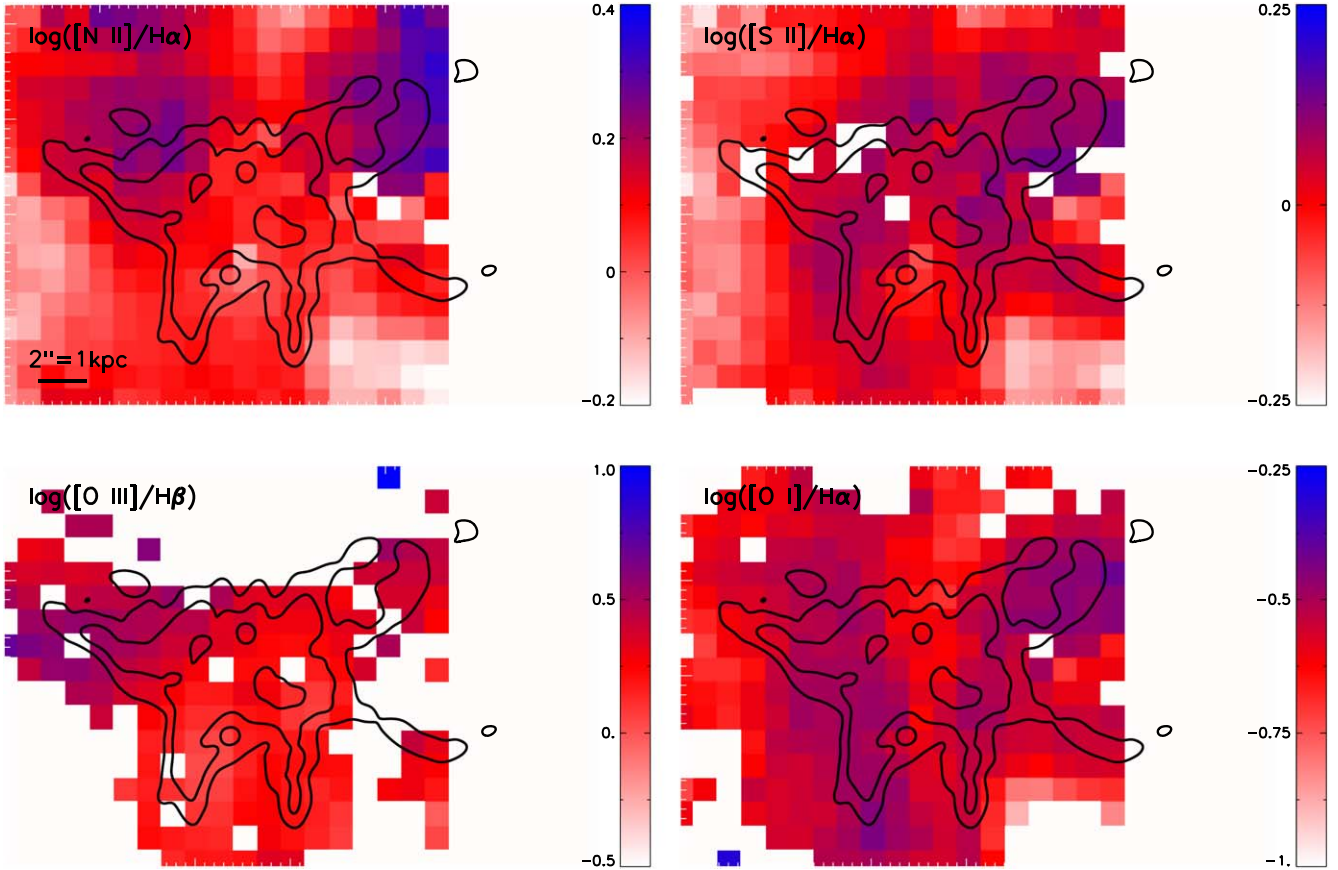


Figure 17. Emission-line ratio maps $[\text{N II}]/\text{H}\alpha$, $[\text{S II}]/\text{H}\alpha$, $[\text{O I}]/\text{H}\alpha$, and $[\text{O III}]/\text{H}\beta$ constructed from WiFeS seeing-limited integral field spectroscopy. By spectrally separating $\text{H}\alpha$ and $[\text{N II}]$, we see an enhancement of $[\text{S II}]/\text{H}\alpha$ and $[\text{O I}]/\text{H}\alpha$ along the filaments that was not evident in the HST data set shown in Figure 5.

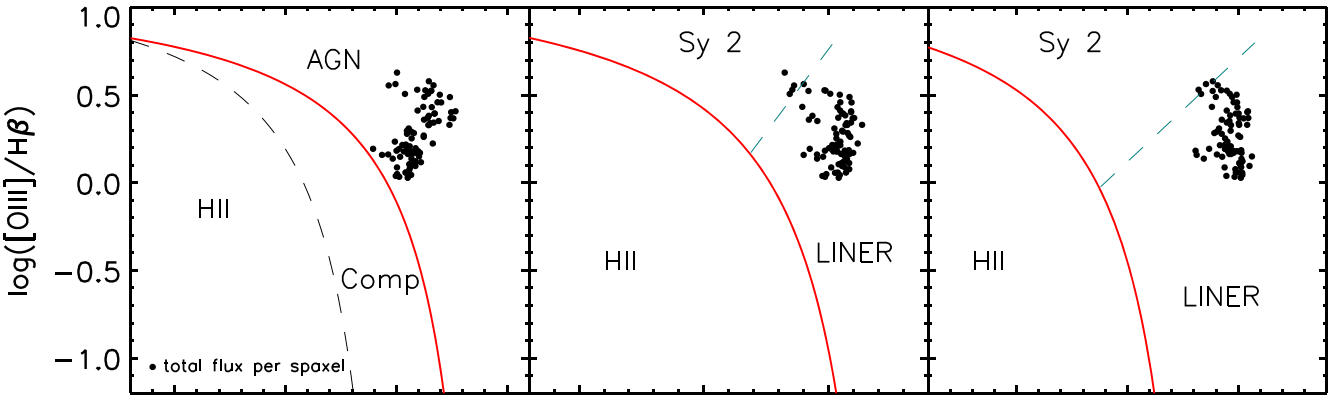


Figure 18. Emission-line diagnostic diagrams from Baldwin et al. (1981) and Veilleux & Osterbrock (1987) and classification lines from Kewley et al. (2006) for each spaxel of our WiFeS integral field spectroscopy data. In each panel, each point shows the summed flux from all Gaussian components fit to each emission line. Data are only shown if all relevant emission lines have a $S/N > 5$. As expected from previous unresolved spectra, most of NGC 6240's emission is dominated by LINER-like line ratios, most likely due to shocks caused by the ongoing outflows. The diagnostic diagrams show a shock-mixing sequence (extending from bottom left toward top right of each panel) with an upturn toward the top left where the high $[\text{O III}]/\text{H}\beta$ ratio suggests AGN-like photoionization.

falling in the LINER classification region from Kewley et al. (2006). We see evidence of a shock-mixing sequence extending from lower line ratios to higher in all three panels, likely demonstrating spatial regions where ionization from outflow-induced shocks dominates more (top right) or less (bottom left) over star formation (Rich et al. 2011; Davies et al. 2017; D’Agostino et al. 2018). A small turn to the upper left is caused by the high $[\text{O III}]/\text{H}\beta$ ratio seen in the eastern arm discussed in Section 6.

ORCID iDs

- Anne M. Medling [ID](https://orcid.org/0000-0001-7421-2944) <https://orcid.org/0000-0001-7421-2944>
- Lisa J. Kewley [ID](https://orcid.org/0000-0001-8152-3943) <https://orcid.org/0000-0001-8152-3943>
- Daniela Calzetti [ID](https://orcid.org/0000-0002-5189-8004) <https://orcid.org/0000-0002-5189-8004>
- George C. Privon [ID](https://orcid.org/0000-0003-3474-1125) <https://orcid.org/0000-0003-3474-1125>
- Kirsten Larson [ID](https://orcid.org/0000-0003-3917-6460) <https://orcid.org/0000-0003-3917-6460>
- Jeffrey A. Rich [ID](https://orcid.org/0000-0002-5807-5078) <https://orcid.org/0000-0002-5807-5078>
- Lee Armus [ID](https://orcid.org/0000-0003-3498-2973) <https://orcid.org/0000-0003-3498-2973>
- Mark G. Allen [ID](https://orcid.org/0000-0003-2168-0087) <https://orcid.org/0000-0003-2168-0087>

Geoffrey V. Bicknell [ID](https://orcid.org/0000-0003-0234-7940) <https://orcid.org/0000-0003-0234-7940>
 Tanio Díaz-Santos [ID](https://orcid.org/0000-0003-0699-6083) <https://orcid.org/0000-0003-0699-6083>
 Timothy M. Heckman [ID](https://orcid.org/0000-0001-6670-6370) <https://orcid.org/0000-0001-6670-6370>
 Claus Leitherer [ID](https://orcid.org/0000-0003-2685-4488) <https://orcid.org/0000-0003-2685-4488>
 Claire E. Max [ID](https://orcid.org/0000-0003-0682-5436) <https://orcid.org/0000-0003-0682-5436>
 David S. N. Rupke [ID](https://orcid.org/0000-0002-1608-7564) <https://orcid.org/0000-0002-1608-7564>
 Ezequiel Treister [ID](https://orcid.org/0000-0001-7568-6412) <https://orcid.org/0000-0001-7568-6412>
 Hugo Messias [ID](https://orcid.org/0000-0002-2985-7994) <https://orcid.org/0000-0002-2985-7994>
 Alexander Y. Wagner [ID](https://orcid.org/0000-0002-5104-6434) <https://orcid.org/0000-0002-5104-6434>

References

- Aird, J., Nandra, K., Laird, E. S., et al. 2010, *MNRAS*, **401**, 2531
 Allen, M. G., Groves, B. A., Dopita, M. A., Sutherland, R. S., & Kewley, L. J. 2008, *ApJS*, **178**, 20
 Armus, L., Bernard-Salas, J., Spoon, H. W. W., et al. 2006, *ApJ*, **640**, 204
 Baan, W. A., Hagiwara, Y., & Hofner, P. 2007, *ApJ*, **661**, 173
 Baldwin, J. A., Phillips, M. M., & Terlevich, R. 1981, *PASP*, **93**, 5
 Banda-Barragán, W., Brüggen, M., Heesen, V., et al. 2020, *MNRAS*, **506**, 5658
 Beirão, P., Armus, L., Lehnert, M. D., et al. 2015, *MNRAS*, **451**, 2640
 Brüggen, M., & Scappapietra, E. 2016, *ApJ*, **822**, 31
 Cappellari, M., & Emsellem, E. 2004, *PASP*, **116**, 138
 Childress, M. J., Vogt, F. P. A., Nielsen, J., & Sharp, R. G. 2014, *Ap&SS*, **349**, 617
 Cicone, C., Maiolino, R., Sturm, E., et al. 2014, *A&A*, **562**, A21
 Cicone, C., Severgnini, P., Papadopoulos, P. P., et al. 2018, *ApJ*, **863**, 143
 Colbert, E. J. M., Wilson, A. S., & Bland-Hawthorn, J. 1994, *ApJ*, **436**, 89
 D'Agostino, J. J., Kewley, L. J., Groves, B. A., et al. 2019, *MNRAS*, **485**, L38
 D'Agostino, J. J., Poetrodjojo, H., Ho, I.-T., et al. 2018, *MNRAS*, **479**, 4907
 Davies, R. I., Sternberg, A., Lehnert, M., & Tacconi-Garman, L. E. 2003, *ApJ*, **597**, 907
 Davies, R. L., Groves, B., Kewley, L. J., et al. 2017, *MNRAS*, **470**, 4974
 Dopita, M., Hart, J., McGregor, P., et al. 2007, *Ap&SS*, **310**, 255
 Dopita, M., Rhee, J., Farage, C., et al. 2010, *Ap&SS*, **327**, 245
 Doyon, R., Wright, G. S., & Joseph, R. D. 1994, *ApJ*, **421**, 115
 Engel, H., Davies, R. I., Genzel, R., et al. 2010, *A&A*, **524**, A56
 Feruglio, C., Fiore, F., Maiolino, R., et al. 2013a, *A&A*, **549**, A51
 Feruglio, C., Fiore, F., Piconcelli, E., et al. 2013b, *A&A*, **558**, A87
 Garmire, G. P., Bautz, M. W., Ford, P. G., Nousek, J. A., & Ricker, G. R., Jr. 2003, *Proc. SPIE*, **4851**, 28
 González-Alfonso, E., Fischer, J., Spoon, H. W. W., et al. 2017, *ApJ*, **836**, 11
 Gowardhan, A., Spoon, H., Riechers, D. A., et al. 2018, *ApJ*, **859**, 35
 Guillard, P., Boulanger, F., Pineau Des Forets, G., & Appleton, P. N. 2009, *A&A*, **502**, 515
 Heckman, T. M., Armus, L., & Miley, G. K. 1987, *AJ*, **93**, 276
 Heckman, T. M., Armus, L., & Miley, G. K. 1990, *ApJS*, **74**, 833
 Hill, M. J., & Zakamska, N. L. 2014, *MNRAS*, **439**, 2701
 Hinshaw, G., Weiland, J. L., Hill, R. S., et al. 2009, *ApJS*, **180**, 225
 Ho, I.-T., Kewley, L. J., Dopita, M. A., et al. 2014, *MNRAS*, **444**, 3894
 Ho, I.-T., Medling, A. M., Groves, B., et al. 2016, *Ap&SS*, **361**, 280
 Hollenbach, D., & McKee, C. F. 1980, *ApJL*, **241**, L47
 Hummer, D. G., & Storey, P. J. 1987, *MNRAS*, **224**, 801
 Kartaltepe, J. S., Dickinson, M., Alexander, D. M., et al. 2012, *ApJ*, **757**, 23
 Kartaltepe, J. S., Sanders, D. B., Le Floc'h, E., et al. 2010, *ApJ*, **721**, 98
 Keel, W. C. 1990, *AJ*, **100**, 356
 Kennicutt, R. C., Jr. 1998, *ApJ*, **498**, 541
 Kewley, L. J., Groves, B., Kauffmann, G., & Heckman, T. 2006, *MNRAS*, **372**, 961
 Kewley, L. J., Nicholls, D. C., & Sutherland, R. S. 2019, *ARA&A*, **57**, 511
 Kim, D.-C., Evans, A. S., Vavilkin, T., et al. 2013, *ApJ*, **768**, 102
 Komossa, S., Burwitz, V., Hasinger, G., et al. 2003, *ApJL*, **582**, L15
 Larkin, J. E., Armus, L., Knop, R. A., Soifer, B. T., & Matthews, K. 1998, *ApJS*, **114**, 59
 Larson, K. L., Díaz-Santos, T., Armus, L., et al. 2020, *ApJ*, **888**, 92
 Lutz, D., Sturm, E., Genzel, R., et al. 2003, *A&A*, **409**, 867
 Madau, P., Pozzetti, L., & Dickinson, M. 1998, *ApJ*, **498**, 106
 Marconi, A., Oliva, E., van der Werf, P. P., et al. 2000, *A&A*, **357**, 24
 Markwardt, C. B. 2009, in ASP Conf. Ser. 411, Astronomical Data Analysis Software and Systems XVIII, ed. D. A. Bohlander, D. Durand, & P. Dowler (San Francisco, CA: ASP), 251
 Max, C. E., Canalizo, G., & de Vries, W. H. 2007, *Sci*, **316**, 1877
 Max, C. E., Canalizo, G., Macintosh, B. A., et al. 2005, *ApJ*, **621**, 738
 Medling, A. M., Ammons, S. M., Max, C. E., et al. 2011, *ApJ*, **743**, 32
 Medling, A. M., U. V., Guedes, J., et al. 2014, *ApJ*, **784**, 70
 Medling, A. M., U. V., Rich, J. A., et al. 2015, *MNRAS*, **448**, 2301
 Meijerink, R., Kristensen, L. E., Weiß, A., et al. 2013, *ApJL*, **762**, L16
 Moorwood, A. F. M., van der Werf, P. P., Kotilainen, J. K., Marconi, A., & Oliva, E. 1996, *A&A*, **308**, L1
 Müller-Sánchez, F., Nevin, R., Comerford, J. M., et al. 2018, *Natur*, **556**, 345
 Nardini, E., Wang, J., Fabbiano, G., et al. 2013, *ApJ*, **765**, 141
 Ohyama, Y., Yoshida, M., & Takata, T. 2003, *AJ*, **126**, 2291
 Puxley, P. J., Hawarden, T. G., & Mountain, C. M. 1990, *ApJ*, **364**, 77
 Rich, J. A., Dopita, M. A., Kewley, L. J., & Rupke, D. S. N. 2010, *ApJ*, **721**, 505
 Rich, J. A., Kewley, L. J., & Dopita, M. A. 2011, *ApJ*, **734**, 87
 Roussel, H., Helou, G., Hollenbach, D. J., et al. 2007, *ApJ*, **669**, 959
 Rupke, D. S. N., & Veilleux, S. 2013, *ApJL*, **775**, L15
 Saito, T., Iono, D., Ueda, J., et al. 2018, *MNRAS*, **475**, L52
 Sanders, D. B., & Mirabel, I. F. 1996, *ARA&A*, **34**, 749
 Scappapietra, E., & Brüggen, M. 2015, *ApJ*, **805**, 158
 Schneider, E. E., & Robertson, B. E. 2017, *ApJ*, **834**, 144
 Schneider, E. E., Robertson, B. E., & Thompson, T. A. 2018, *ApJ*, **862**, 56
 Sharp, R. G., & Bland-Hawthorn, J. 2010, *ApJ*, **711**, 818
 Spoon, H. W. W., Farrah, D., Lebouteiller, V., et al. 2013, *ApJ*, **775**, 127
 Sturm, E., González-Alfonso, E., Veilleux, S., et al. 2011, *ApJL*, **733**, L16
 Sutherland, R. S., & Dopita, M. A. 2017, *ApJS*, **229**, 34
 Tacconi, L. J., Genzel, R., Tecza, M., et al. 1999, *ApJ*, **524**, 732
 Tecza, M., Genzel, R., Tacconi, L. J., et al. 2000, *ApJ*, **537**, 178
 Thompson, T. A., Quataert, E., Zhang, D., & Weinberg, D. H. 2016, *MNRAS*, **455**, 1830
 Treister, E., Messias, H., Privon, G. C., et al. 2020, *ApJ*, **890**, 149
 U. V., Medling, A. M., Inami, H., et al. 2019, *ApJ*, **871**, 166
 van Dam, M. A., Le Mignant, D., & Macintosh, B. A. 2004, *ApOpt*, **43**, 5458
 van der Werf, P. P., Genzel, R., Krabbe, A., et al. 1993, *ApJ*, **405**, 522
 Veilleux, S., Kim, D.-C., & Sanders, D. B. 2002, *ApJS*, **143**, 315
 Veilleux, S., Meléndez, M., Sturm, E., et al. 2013, *ApJ*, **776**, 27
 Veilleux, S., & Osterbrock, D. E. 1987, *ApJS*, **63**, 295
 Veilleux, S., Rupke, D. S. N., & Swaters, R. 2009, *ApJL*, **700**, L149
 Veilleux, S., Shopbell, P. L., Rupke, D. S., Bland-Hawthorn, J., & Cecil, G. 2003, *AJ*, **126**, 2185
 Wagner, A. Y., Umemura, M., & Bicknell, G. V. 2013, *ApJL*, **763**, L18
 Walter, F., Weiss, A., & Scoville, N. 2002, *ApJL*, **580**, L21
 Wang, J., Nardini, E., Fabbiano, G., et al. 2014, *ApJ*, **781**, 55
 Weaver, R., McCray, R., Castor, J., Shapiro, P., & Moore, R. 1977, *ApJ*, **218**, 377
 Wizinowich, P. L., Acton, D. S., Lai, O., et al. 2000, *Proc. SPIE*, **4007**, 2
 Wright, E. L. 2006, *PASP*, **118**, 1711
 Yoshida, M., Yagi, M., Ohyama, Y., et al. 2016, *ApJ*, **820**, 48
 Yun, M. S., Hibbard, J. E., Condon, J. J., & Reddy, N. 1999, *Ap&SS*, **266**, 29